

Conductance Model for Extreme Events : Impact of Auroral Conductance on Space Weather Forecasts

Agnit Mukhopadhyay¹, Daniel T. Welling², Michael W. Liemohn¹, Aaron J. Ridley¹, Shibaji Chakraborty³, and Brian J. Anderson⁴

¹Climate and Space Sciences and Engineering Department, University of Michigan, Ann Arbor, MI, USA

²Department of Physics, University of Texas at Arlington, Arlington, TX, USA

³Department of Electrical and Computer Engineering, Virginia Polytechnic Institute and State University, Blacksburg, VA, USA

⁴Applied Physics Laboratory, Johns Hopkins University, Baltimore, MD, USA

Key Points:

- An updated auroral conductance module is built for global models using nonlinear regression & empirical adjustments spanning extreme events.
- Expanded dataset raises the ceiling of conductance values, impacting the polar cap potential, dB/dt & ΔB predictions during extreme events.
- Application of expanded model with empirical oval adjustments refines the conductance pattern, and drastically improves dB/dt predictions.

This is the author manuscript accepted for publication and has undergone full peer review but has not been through the copyediting, typesetting, pagination and proofreading process, which may lead to differences between this version and the Version of Record. Please cite this article

as doi: [10.1029/2020SW002551](https://doi.org/10.1029/2020SW002551)

Corresponding author: Agnit Mukhopadhyay, agnitm@umich.edu

Abstract

Ionospheric conductance is a crucial factor in regulating the closure of magnetospheric field-aligned currents through the ionosphere as Hall and Pedersen currents. Despite its importance in predictive investigations of the magnetosphere - ionosphere coupling, the estimation of ionospheric conductance in the auroral region is precarious in most global first-principles based models. This impreciseness in estimating the auroral conductance impedes both our understanding and predictive capabilities of the magnetosphere-ionosphere system during extreme space weather events. In this article, we address this concern, with the development of an advanced Conductance Model for Extreme Events (CMEE) that estimates the auroral conductance from field aligned current values. CMEE has been developed using nonlinear regression over a year's worth of one-minute resolution output from assimilative maps, specifically including times of extreme driving of the solar wind-magnetosphere-ionosphere system. The model also includes provisions to enhance the conductance in the aurora using additional adjustments to refine the auroral oval. CMEE has been incorporated within the Ridley Ionosphere Model (RIM) of the Space Weather Modeling Framework (SWMF) for usage in space weather simulations. This paper compares performance of CMEE against the existing conductance model in RIM, through a validation process for six space weather events. The performance analysis indicates overall improvement in the ionospheric feedback to ground-based space weather forecasts. Specifically, the model is able to improve the prediction of ionospheric currents which impact the simulated dB/dt and ΔB , resulting in substantial improvements in dB/dt predictive skill.

Plain Language Summary

Electric currents generated in the Earth's space environment due to its magnetic interaction with the Sun leads to charged particle deposition and closure of these currents in the terrestrial upper atmosphere, especially in the high latitude auroral region. The enhancement in the electrical charge carrying capacity as a result of this process in the Earth's upper atmosphere, also known as the ionosphere, is challenging to estimate in most numerical simulations attempting to study the interactive dynamic and chemical processes in the near-Earth region. The inability to accurately estimate this quantity leads to underprediction of severe space weather events that can have adverse impacts on man-made technology like electrical power grids, railway and oil pipelines. In this study, we present a novel modeling approach to address this problem, and provide global simulations with a more accurate estimate on the electrical conductivity of the ionosphere. Through this investigation, we show that the accurate measurement of the charge carriers in the ionosphere using the new model causes substantial improvements in the prediction of space weather on the ground, and significantly advances our understanding of global dynamics causing ground-based space weather.

1 Introduction

The interaction of the solar wind and the terrestrial magnetic field produces magnetospheric current systems such as field aligned currents (FACs) which close through the conductive ionosphere, thereby allowing magnetospheric convection to eventuate (e.g. Axford & Hines, 1961; Dungey, 1963; Iijima & Potemra, 1976). For precise investigations of the magnetospheric feedback on the ionosphere and vice versa, an accurate estimate of the ionospheric conductance is critical for realistic global modeling of the magnetosphere, especially during space weather events (e.g. Merkin et al., 2003, Ridley et al., 2004, Merkin, Sharma, et al., 2005; Merkin, Milikh, et al., 2005, Liemohn et al., 2005). Two dominant sources contribute to the ionosphere's enhanced but finite conductivity - solar extreme ultra-violet (EUV) flux on the dayside, and auroral precipitation in the polar region predominantly on the nightside (Schunk & Nagy, 2009; Newell et al., 2009;

67 Fuller-Rowell & Evans, 1987). Conductance due to solar EUV radiation is relatively well
68 understood through the use of radiative transfer (e.g. Chapman, 1931). The EUV flux
69 is accounted for in most modern modeling tools as a physics-based empirical function
70 of the solar zenith angle (e.g., Brekke & Moen 1993). Auroral electron and ion precipi-
71 tation, largely driven by magnetospheric processes, further ionizes neutrals and ions in
72 the ionosphere (e.g., Frahm et al., 1997; Ahn et al., 1998), and enhances the electrical
73 conductivity in the high-latitude auroral regions (Robinson et al., 1987). Since auroral
74 precipitation of charged particles is directly related to variations in the intrinsic mag-
75 netic field (e.g., Roederer, 1970), auroral conductance is an important quantity to pre-
76 dict when investigating the ionosphere’s impact on the magnetosphere, and vice versa,
77 during strong driving when the global magnetic field changes rapidly (e.g., Welling, 2019).

78 Although several studies have examined the influence of the ionospheric conduc-
79 tance on the global state of the magnetosphere, ionospheric dynamics and their coupled
80 non-linear feedback system (e.g., Raeder et al., 2001; Ridley et al., 2001, 2004; Liemohn
81 et al., 2005; Wiltberger et al., 2001, 2004; Zhang et al., 2015; Connor et al., 2016; Oz-
82 turk et al., 2017), few studies have actually explored the contribution of conductance on
83 space weather forecasts (e.g. Hartinger et al., 2017), especially during extreme space weather
84 events. This is very difficult to do with data, since measurements of the ionospheric conduc-
85 tance are notoriously inaccurate (Ohtani et al., 2014). Investigations using global mod-
86 els such as Ridley et al. (2004) have indulged in the broad quantification of the conduc-
87 tance due to EUV illumination and auroral precipitation. Studies such as Wiltberger et
88 al. (2001), Zhang et al. (2015), Yu et al. (2016) and Wiltberger et al. (2017) addressed
89 this further by identifying the source and impact of various contributors to the auroral
90 conductance. Additional evaluations by Perlongo et al. (2017) included the effect of auro-
91 ral precipitation due to the ring current using a kinetic ring current model coupled to
92 an ionosphere-thermosphere model. Modeling efforts by Ahn et al. (1998), Newell et al.
93 (2009), Korth et al. (2014) have estimated ionospheric auroral conductance through em-
94 pirical relations, using global quantities like solar wind input, ground-based magnetic per-
95 turbations and field aligned currents as inputs. The Robinson conductance model (Robin-
96 son et al., 1987; Kaeppeler et al., 2015) relating downward precipitating fluxes to auro-
97 ral conductance is yet another prominent example of empirically-derived conductance
98 from global magnetospheric quantities. Recently, Robinson et al. (2018) developed an
99 empirical model using incoherent scatter radar measurements against AMPERE FAC
100 estimations, which spanned the St. Patrick’s Day Storm of 2015, an event studied exten-
101 sively for ionospheric disturbances (e.g., Le et al., 2016). In spite of its importance,
102 the impact of auroral conductance during extreme events in global simulations has been
103 hard to determine, due to inaccuracies in conductance estimations within global mod-
104 els, leading to possible underprediction of global quantities like cross polar cap poten-
105 tial (e.g., Honkonen et al., 2013; Mukhopadhyay, 2017), field aligned currents (Anders-
106 son et al., 2017), storm indices (Liemohn, McCollough, et al., 2018) and transient ground-
107 based magnetic perturbations (Welling et al., 2018).

108 With rising operational usage of first-principles-based geospace models in space weather
109 prediction, the need for accurate conductance models is even more necessary. Operational
110 forecasts of the near-Earth space environment using first-principles based global numer-
111 ical frameworks (e.g., Tóth et al., 2005), combining global magnetohydrodynamic (MHD)
112 models (e.g., Powell et al., 1999; Raeder et al., 2001) with suitable inner magnetospheric
113 models (e.g., De Zeeuw et al., 2004) and ionospheric models (e.g., Ridley & Liemohn,
114 2002; Wiltberger et al., 2004), have been in use for space weather prediction (Liemohn,
115 Ganushkina, et al., 2018) since the end of the GEM Challenge of 2008-09 (Pulkkinen et
116 al., 2011, 2013, Rastaetter et al. 2013). The procedural assessment specifically presented
117 in Pulkkinen et al. (2013) (hereinafter referred to as *Pulkkinen2013*) to investigate pre-
118 dictive skill of global first-principles-based models in predicting ground-based magnetic
119 perturbations dB/dt , initiated the transition of model usage toward operational predic-
120 tion at the NOAA Space Weather Prediction Center (SWPC). Several investigations, since

121 then, have further reviewed and systematically addressed the results from this effort, and
122 have suggested rectifications to improve predictive skill (e.g., Honkonen et al., 2013; Glo-
123 cker et al., 2016; Anderson et al., 2017; Mukhopadhyay, 2017; Liemohn, Ganushkina, et
124 al., 2018; Liemohn, McCollough, et al., 2018; Welling et al., 2018). In particular, the study
125 by Welling et al. (2017) indicated inherent deficiencies in auroral conductance models
126 used in global models that inhibited them from estimating conductance accurately dur-
127 ing extreme space weather events. The study concluded that the inability of global mod-
128 els to estimate the ionospheric conductance accurately during extreme events led to un-
129 derprediction of dB/dt .

130 A key conclusion in the study by Welling et al. (2017) (hereinafter referred to as
131 *Welling2017*) questions the dataset used in estimating a geospace model’s auroral con-
132 ductance during extreme weather, and hypothesizes that the inclusion of information from
133 a larger dataset, including sufficient coverage of extreme events, may lead to improve-
134 ments in a model’s space weather predictive metrics during extreme events. The study
135 falls short of addressing supplementary effects due to the auroral oval’s pattern estima-
136 tion in aforementioned models, and the acute effect such a pattern may have on predic-
137 tive skill. In this paper, we describe the development and validation of an updated em-
138 pirical auroral conductance model, specifically including data that spans several extreme
139 events, which addresses the concerns raised in *Welling2017*. We use this conductance model
140 within the geospace variant of the Space Weather Modeling Framework (SWMF; Tóth
141 et al., 2005, 2012), identical to the version used operationally at the NOAA Space Weather
142 Prediction Center for space weather forecasting, to investigate the effect of this enhanced
143 conductance model on space weather predictions, and compare these results to the already-
144 existing conductance model within the SWMF. We additionally study the effect of ad-
145 justing the pattern of the auroral oval using empirical enhancements based on field aligned
146 current strength, to alter the model’s space weather predictions. As a result, in this ar-
147 ticle, we investigate three major science questions:

- 148 1. Addressing *Welling2017*: Does expanding the dataset used to create the initial
149 conductance model help improve space weather predictions?
- 150 2. How significant is the improvement in the space weather predictions due to the
151 enhanced auroral oval adjustment parameters?
- 152 3. Can the combination of the expanded dataset and an auroral oval enhancement
153 cause significant improvement in the global model’s space weather prediction?

154 In order to address the aforementioned questions, a new **Conductance Model for Extreme**
155 **Events** (CMEE) has been developed. CMEE is based on the SWMF’s empirical auro-
156 ral conductance model, which uses an inverse-exponential relation to estimate the con-
157 ductance, and employs an empirically-driven auroral oval adjustment to enhance con-
158 ductance in regions of strong FACs. A key difference in CMEE, however, is in the dataset
159 it was developed from: CMEE uses one whole year of AMIE data to estimate its con-
160 ductance. Compared to the old model which was derived from the relatively quiet month
161 of January 1997, minute-data from the whole year of 2003 was utilized to develop CMEE.
162 This included some of the most extreme geospace events ever observed (Cid et al., 2015).
163 In addition to an enlarged training dataset, the value of the empirical coefficients in CMEE
164 are deduced using a non-linear fitting algorithm with suitable extreme boundary con-
165 ditions that minimizes the absolute error and maximizes the prediction efficiency. The
166 global model configurations used and the science questions addressed in this study, and
167 the subsequent results from this study are described in Sections 2 and 3 respectively, while
168 the algorithm used to develop the advance conductance model and the auroral oval ad-
169 justment module have been described in Section 2.2.

2 Methodology

2.1 Simulation Setup

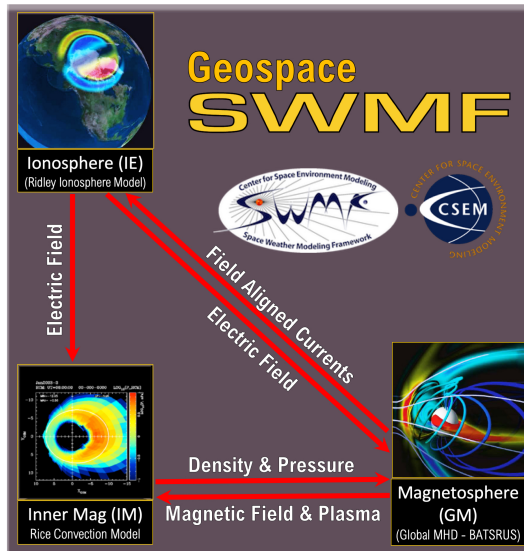


Figure 1. Component layout of the geospace version of the SWMF, same as the layout in *Pulkkinen2013*, used in this study to investigate the role of auroral conductance in space weather prediction.

The SWMF is a flexible framework that executes, synchronizes and couples many otherwise independent models together as one. It has performed favorably in predictive metric challenges and investigations (e.g., *Pulkkinen2013*; Honkonen et al., 2013; Mukhopadhyay, 2017; Welling et al., 2017; Liemohn, McCollough, et al., 2018), contains an easily-modifiable empirical conductance model in the ionospheric electrodynamic module (Ridley et al., 2004), and is capable of calculating perturbations to the magnetic field (ΔB) by applying Biot-Savart integrals across its domain to estimate magnetometer values virtually (Yu et al., 2010). For this study, we have used the SWMF with three physical modules activated (Figure 1; details below). Identical to the study conducted by *Pulkkinen2013*, the SWMF’s geospace version was configured to use three components: Global Magnetosphere (GM), Inner Magnetosphere (IM), and Ionospheric Electrodynamics (IE).

The GM module uses the Block Adaptive Tree Solar-Wind Roe Upwind Scheme (BATS-R-US, Powell et al., 1999; Gombosi et al., 2003) model which solves for the ideal non-relativistic magnetohydrodynamic (MHD) equations in the magnetosphere with an inner boundary at $\sim 2.5 R_E$. The computational domain for geospace simulations of BATS-R-US extends from $32R_E$ upstream to $-224R_E$ downstream in the x direction and $128R_E$ in the y and z coordinates (GSM). The key feature of BATS-R-US is its flexible, block-adaptive Cartesian grid that reserves the highest resolution to regions of interest, ensuring the best combination of performance and accuracy.

The IM region is characterized by closed magnetic field lines and particles of keV energies. This module uses Rice Convection Model (RCM; Wolf et al., 1982). RCM solves for the bounce averaged and isotropic but energy resolved particle distribution of electrons and various ions. RCM receives flux tube volumes from BATS-R-US and returns the pressure and density values to correct those calculated within GM (De Zeeuw et al., 2004). It receives the ionospheric electric potential from the 2-dimensional IE module.

197 The density and temperature initial and boundary values are computed from the GM
198 solution.

199 The IE component calculates height integrated ionospheric quantities at an alti-
200 tude of about 110 km. To do so, it receives field aligned currents (FACs) from GM and
201 uses the Ridley Ionosphere Model (RIM, Ridley et al. 2001; Ridley & Liemohn 2002; Ri-
202 dley et al. 2004), a finite-difference Poisson solver, to calculate the electric potential and
203 horizontal currents using a *prescribed* but dynamic conductance pattern. The module
204 maps FACs at 3.5 Earth radii (R_E) over a two dimensional ionospheric domain, solves
205 for the resulting potential using Ohm's Law (Goodman, 1995), and returns this value
206 to GM and IM. The functioning of and developments to the ionospheric conductance model
207 of RIM are the key features of this article, and are discussed in detail in Section 2.2, along
208 with the development of a more advanced empirical conductance model, CMEE, as a re-
209 placement to the aforementioned model.

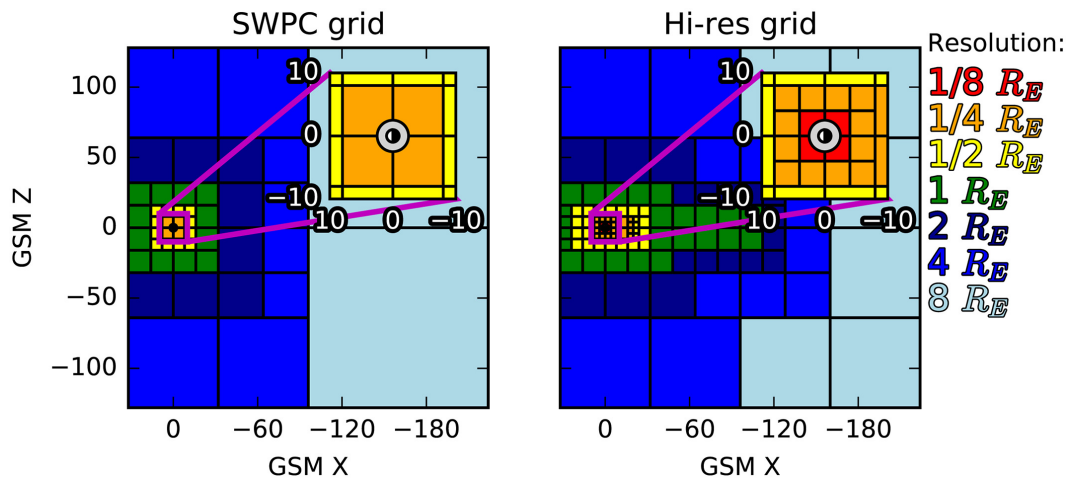


Figure 2. X-Z cuts showing cell sizes in the two MHD grids (reproduced from Haiducek et al., 2017). (Left) The grid used for the *SWPC* configuration (minimum cell size of $0.25 R_E$). (Right) The higher-resolution grid used for the *Hi-Res SWPC* configuration (minimum cell size of $0.125 R_E$)

210 In order to simulate a given event, we drive the model using solar wind velocity,
211 magnetic field, density, and temperature, which are used to specify the upstream bound-
212 ary condition of BATS-R-US. The only other input parameter is F10.7 flux, which is used
213 by IE in computing the dayside EUV-driven ionospheric conductivity (Moen & Brekke,
214 1993; Ridley et al., 2004). Simulation parameters have been kept similar to *Pulkkinen2013*,
215 throughout the study; the model input conditions and parameters are not tailored to in-
216 dividual events. The same solar wind values derived in *Pulkkinen2013* from instruments
217 onboard the Advanced Composition Explorer (ACE) satellite were used to drive simu-
218 lations in the present study. For this study, we have simulated the events using two dif-
219 ferent resolutions of BATS-R-US : *SWPC* and *Hi-Res SWPC* (see Figure 2). The *SWPC*
220 configuration is nearly identical to the *Pulkkinen2013* study, and is used operationally
221 by the Space Weather Prediction Center (SWPC). This grid (Figure 2, left) has cell sizes
222 ranging from $8 R_E$ in the distant tail to $0.25 R_E$ at the inner boundary, a $16 R_E$ diam-
223 eter cube surrounding the Earth, and contains around 1 million cells. The other configu-
224 ration, *Hi-Res SWPC*, is similar to the previous configuration but uses a higher-resolution
225 grid (among other modifications), to help resolve field aligned currents at the spatial in-
226 ner boundary. The cell size of this grid (Figure 2, right) varies from $8 R_E$ in the tail to

0.125 R_E near the Earth, and contains ~ 1.9 million cells. Both configurations use a 91×181 cell configuration in the IE domain, with a 2 degree cadence in both latitude and longitude. For a detailed description of the above configurations, please refer to Welling & Ridley (2010) and Haiducek et al. (2017).

2.2 Estimation of Auroral Conductance in SWMF

For Ohm's Law to be solved within IE, knowledge of the ionospheric conductance tensor must be known *a priori* (e.g., Goodman, 1995). Within RIM, the legacy code estimating the ionospheric conductance (Ridley et al., 2004) distinguishes two dominant sources of ionospheric conductance: solar EUV conductance on the dayside, and the auroral precipitative conductance in the polar regions. Supplementary sources of conductance, like nightside "starlight" conductance, seasonal dependencies and polar rain, are added as either functions of the dominant sources of conductance, solar zenith angle or scalar constants. The solar EUV component to the conductance is dependent on the absorption and ion production function of the atmosphere as a function of the solar zenith angle, and is therefore straightforward to estimate using radiometry; the model described in Moen & Brekke (1993) is used to estimate this component of the conductance in most global models (e.g. Raeder et al., 2001 Wiltberger et al., 2004), including RIM. The conductance due to ion and electron precipitation in the auroral region is harder to predict, as this would require the precise knowledge of the charged particle distribution in the magnetosphere. While a physics-based approach to precipitation has been applied in several global models (e.g. Raeder et al., 2001, Zhang et al., 2015, Yu et al., 2016, Perlongo et al., 2017) using kinetic theory (e.g. Knight, 1973), RIM uses a different and simpler approach to estimate the auroral conductance.

2.2.1 Functioning of the Ridley Legacy Model

The auroral conductance module in RIM (briefly described in Ridley et al., 2004), hereinafter referred to as the Ridley Legacy Model (RLM), uses the magnitude and direction of modelled FACs to empirically determine the auroral conductance. This is similar to existing statistical models constructed using FACs to predict and examine precipitation in the auroral ionosphere (e.g. Ahn et al., 1998, Korth et al., 2014, Carter et al., 2016, Robinson et al., 2018). While the numerical domain of RIM spans the entire ionosphere, the RLM domain is considerably limited, spanning from the magnetic pole to magnetic latitude of 60° for all magnetic local times (MLT). The auroral conductance at a given magnetic latitude and MLT is assumed to have the form:

$$\Sigma_{HorP} = A_0 - A_1 e^{-A_2^2 |J_{||}|} \quad (1)$$

where Σ_{HorP} denotes the auroral Hall or Pedersen Conductance in the ionosphere (in siemens), $J_{||}$ denotes the field aligned current density (in $\mu A/m^2$), and A_0 , A_1 (in siemens) and A_2 (in $m/\mu A^{-1/2}$) are fitting coefficients dependent on location. Note that this inverse exponential relation is different from the one mentioned in Ridley et al. (2004); this was a typographical error and the actual relation is given by Equation 1.

The empirical coefficients are the result of fitting based off of conductance and field-aligned current maps derived from assimilative maps of ionospheric electrodynamics (AMIE; Richmond & Kamide, 1988; Kihn & Ridley, 2005) for the month of January 1997 (Booniriseth et al., 2001), using ground magnetic perturbations from ~ 150 ground-based magnetometers. AMIE derives the auroral conductance using the formulation in Ahn et al. (1998) and Lu et al. (1997), which relate ground-based magnetic perturbations to the Hall and Pedersen conductance, and FACs. The exact parameters and version of AMIE used in the development of RLM, with further information about the datasets used have been described in detail in Kihn & Ridley (2005). The month of runs encompasses $\sim 45,000$ two-dimensional maps of Hall and Pedersen conductance and field-aligned currents. In addition to the empirical maps defining the conductance using FACs, additional auro-

267 ral oval adjustments were applied to constrain and enhance the conductance in regions
268 of strong FAC driving.

269 **2.2.2 Conductance Adjustments in the Auroral Oval**

270 The conductance pattern in RLM tends to produce broad regions of high conduc-
271 tance that are discontinuous between regions of strong FACs. To improve upon this, an
272 adjustment to the conductance pattern is applied to the estimated pattern described above.
273 The purpose of this is to create a channel for electrojets to form in the model and to im-
274 prove on the overall electrodynamic result. Though this feature has been implemented
275 in RLM for over a decade, this work is the first to formally describe it and evaluate its
276 impact.

The algorithm for this adjustment starts by estimating the location of the auro-
ral oval. The location of the oval is updated at each simulation timestep of the ionosphere.
Across all local time values (ϕ) in the model's grid, the geomagnetic co-latitude of the
maximum upward FAC at that local time slice ($J_{max}(\phi)$) is obtained. The result is $\theta(\phi)$,
or co-latitude as a function of local time. The mean co-latitude, θ_{mean} , weighted by $J_{max}(\phi)$,
is then obtained as follows:

$$\theta_{mean} = \frac{\sum \theta(\phi) J_{max}(\phi)}{\sum J_{max}(\phi)} \quad (2)$$

A day-night shift in the center of the oval is calculated using the co-latitudes of $J_{max}(\phi)$
at noon and midnight:

$$\Delta\theta = \frac{J_{noon} \times (\theta_{noon} - \theta_{mean}) - J_{midnight} \times (\theta_{midnight} - \theta_{mean})}{J_{noon} + J_{midnight}} \quad (3)$$

Using these values, the location of the auroral oval is modeled as follows:

$$\theta(\phi)_{aurora} = \theta_{mean} + \Delta\theta \cos(\phi) \quad (4)$$

With the oval location set, an adjustment is applied to the conductance values about
the oval by adjusting the fitting coefficients, A_0 and A_1 :

$$A_{0,adj} = A_0 e^{-\frac{d^2}{W^2}} \quad (5)$$

$$A_{1,adj} = A_0 - (A_0 - A_1) e^{-\frac{d^2}{W^2}} \quad (6)$$

...where, for each line of constant local time, d is the co-latitude distance from the oval's
locus and W is the width of the oval (default is 2.5°). A baseline conductance about the
oval is also applied to avoid nonphysical solutions in regions of low FACs:

$$\Sigma_{baseline} = 1.7 \times (\Sigma_{HorP} + k e^{-\frac{d^2}{W^2}}) \quad (7)$$

277 where 1.7 is a multiplier meant to amplify the value of the conductance, and k is a con-
278 stant derived from the aggregate value of the AMIE-derived auroral conductance in re-
279 gions of high precipitation (magnetic latitude $\in [65^\circ, 80^\circ]$). The 1.7 multiplier is a legacy
280 value and was chosen for robustness and stability of dB/dt results. In this study, the value
281 of k was found to be 7.5 siemens for Hall conductance, and 5 siemens for Pedersen con-
282 ductance from the AMIE dataset. The net result of this adjustment is that at each timestep,
283 about the oval, the range of possible conductance values is dynamically narrowed and
284 enhanced, and a coherent, sharper auroral conductance pattern arises.

285 **2.2.3 Conductance Model for Extreme Events (CMEE)**

286 Based on the same formulation as RLM, CMEE was developed using a larger dataset
287 in order to include information during intense space weather events ($Dst < -150nT$).

288 For this model, minute-resolution data from AMIE for the whole year of 2003 were uti-
 289 lized to estimate the new fitting coefficients. For consistency, the same version of AMIE
 290 (Kihn & Ridley, 2005) used in the development of RLM has been used for the develop-
 291 ment of CMEE. The use of a year’s worth of minute-data significantly increased the model’s
 292 base dataset from $\sim 45,000$ 2D maps used in RLM, to over $\sim 530,000$ 2D maps used
 293 in the present study. In addition, the year of 2003 included several intense space weather
 294 events. Specifically, the latter half of the year saw some of the largest geomagnetic storms
 295 ever recorded by mankind (e.g. Cid et al., 2015; Doherty et al., 2004), while January
 296 1997 (the month off of which RLM is based) hardly saw any event with a $Dst \leq -100$
 297 nT. In addition to this, the value of the empirical coefficients in CMEE are deduced as-
 298 suming the same empirical relationship between upward or downward FACs with Hall
 299 and Pedersen Conductance, as given by Equation 1. However, unlike RLM which esti-
 300 mates the fitting using equal weighting, the new fitting has been designed using a novel
 301 nonlinear regression algorithm which imposes sufficient boundary conditions to ensure
 302 that the fitted curve extends to these extreme values and is not just limited to the ag-
 303 gregate value of conductance. This was done by basing the max endpoints of the fittings
 304 on the 90% percentile of the FAC values.

Figure 3 (a) presents a representative line plot of Equation 1, and demarcates the
 conductance vs FAC space into bounded regions designed to estimate fitting coefficients.
 The regression algorithm of CMEE classifies FAC data into low and high magnitude bins,
 separately for upward and downward FACs. The bin boundary for low magnitude FACs,
 including zero FACs was based on the approximate order of low magnitude FAC den-
 sity, where asymptotic behavior of conductance values is prevalent and a median value
 could be found. The median value of the conductance populations in this FAC bin is the
 minima of the curve ($A_0 - A_1$). For the low FAC case, setting the bin boundary at $\pm 10^{-4} \mu\text{A}/\text{m}^2$
 for both upward and downward field aligned currents at all locations led to optimum re-
 sults. To deduce the conductance maxima as a constant asymptotic value, the FAC dataset
 was binned into 10 discrete bins with respect to the absolute value of FAC, and the me-
 dian value of conductance in the bin with the highest FAC values (10th bin) was defined
 as A_0 . A Levenburg-Marquadt (e.g. Pujol, 2007) type bounded least-squares method was
 used to estimate the non-linear fitting coefficient A_2 . The fitting error was defined as the
 arithmetic mean of the median absolute percentage error (MAPE) and the median sym-
 metric efficiency (ξ) ratio of the data, as defined in Morley et al. (2018). In order to avoid
 nonphysical solutions from the ionospheric solver due to large gradients (spikiness) in
 the conductance values, a smoothing filter was applied on the coefficients. The filter was
 based on a Laplacian mesh smoothing algorithm (e.g. Herrmann, 1976), commonly used
 in image processing (Yagou et al., 2002) and mesh refinement (Sorkine et al., 2004). The
 filter is applied such that at each node i ,

$$x_i = \begin{cases} x_i & \text{if } \frac{x_i - X}{X} \leq \lambda \\ X & \text{if } \frac{x_i - X}{X} > \lambda \end{cases} \quad (8)$$

where

$$X = \frac{1}{N} \sum_{j=1}^N x_j \quad (9)$$

305 Here, λ is the prescribed difference, N is the number of adjacent vertices to node i , x_j
 306 is the position of the j -th adjacent vertex and x_i is the new position for node i . The pre-
 307 scribed difference, similarly defined as the relative difference, is kept at 10%.

308 Figures 3(b) shows an example of the fitting using the regression algorithm men-
 309 tioned above over a map of Hall conductance and FAC distribution from AMIE, at the
 310 geomagnetic latitude of 62° and MLT 23 for upward FACs. Figure 3(c) compares the fit-
 311 ting function using CMEE’s regression with coefficients from RLM for the same geomag-
 312 netic location, but for both upward and downward FACs. The usage of a regression al-

gorithm over a larger span of data shows visible differences in Figure 3(c), where CMEE, denoted in red, is able to push the max value of the conductance to better estimate the quantity during extreme driving. In addition, because of the usage of low FAC bins, the model is also able to provide uniformity in conductance values when field aligned currents are low and/or switch directions. This was previously not included in RLM, denoted in blue in Figure 3(c), as the coefficient values were estimated using uniform weighting on a case-by-case basis separately for upward and downward FACs.

2.3 Event Selection & Prediction Assessment

In order to evaluate CMEE's predictive capabilities and address the science questions mentioned in Section 1, we have simulated a range of space weather events listed in Table 1(a) using variations of the auroral conductance model within the SWMF for comparisons against observations. Since it is a de-facto standard in the space weather community, the present investigation chose to simulate the same events listed in Table 1 of the *Pulkkinen2013* study. Simulation of these events was administered for the two resolutions described in Section 2.1, and using four different variations of the conductance model :-

1. Using only the empirical coefficients of RLM to specify the aurora,
2. Using only the empirical coefficients of CMEE to specify the aurora,
3. Adjusting RLM estimates with the additional enhancements in the auroral oval, and
4. Adjusting CMEE estimates with the additional enhancements in the auroral oval.

Table 1(b) lists the 8 sets of simulations resulting from the above combination.

The study uses data from satellite in-situ measurements and ground-based observations for comparisons against model results. Cross polar cap potential (CPCP) from the model variants was compared against values obtained via the AMIE model and observations from the Super Dual Auroral Radar Network (SuperDARN; e.g. Khachikjan et al., 2008). Since AMIE has a tendency to overpredict CPCP (e.g. Gao, 2012), observations from the SuperDARN were also used to provide a range to the CPCP estimates. Integrated field aligned currents derived from observations by the Active Magnetosphere and Planetary Electrodynamics Response Experiment (AMPERE) mission (Anderson et al., 2014; Waters et al., 2020), estimated using the methodology in Anderson et al. (2017), were used to compare modeled values of FACs. In addition, magnetometer observations from the 12 magnetometer stations listed in Table 2 of the *Pulkkinen2013* study were used to evaluate the predicted ground-based magnetic perturbation ΔB and its temporal variant dB/dt .

Using a similar approach as *Pulkkinen2013*, a binary event analysis (e.g. Jolliffe & Stephenson, 2012; Wilks, 2011) was used to construct a set of relevant performance metrics. An event is defined as the absolute value of a parameter-in-question (any physical quantity like dB/dt) exceeding a predetermined event threshold at any time within a comparison window t_f . For each such window, four outcomes are possible: "Hit" or True Positive (TP; event is observed, and also predicted), "False Alarm" or False Positive (FP; event is not observed, but predicted by model), "Miss" or False Negative (FN; event is observed, but not predicted), and "Correct No Events" or True Negative (TN; event is not observed, and not predicted). Similar to *Pulkkinen2013*, the analysis forecast window t_f was selected to be 20 minutes. The combined results from all events listed in Table 1(a) for a given simulation set are divided into discrete events by the forecast window, creating a contingency table accounting for TPs, FPs, FNs and TNs for a specific threshold. Unlike the *Pulkkinen2013* study, this study chose to discretize the dB/dt into thresholds ranging from 0.1 nT/s to 1.7 nT/s at intervals of 0.1 nT/s, including the thresholds 0.3 nT/s, 0.7 nT/s, 1.1 nT/s and 1.5 nT/s which were used in the former study.

In addition to dB/dt , the ΔB values have been discretized using thresholds obtained from Tóth et al. (2014) and *Welling2017*, ranging from 75 to 400 nT at intervals of 25 nT were used.

Once the contingency tables were prepared for each simulation variation, a combination of performance metrics were applied to study improvements. The metrics used in this study and their respective definitions are listed in Table 2. Amongst these metrics, the top four are accuracy measures that help describe the improvement of individual outcomes in a contingency table, while the bottom four metrics quantify the accuracy of a prediction. The Probability of Detection (POD), also called the Positive Prediction Value, is the ratio of positive and negative results, and ranges from 0 to 1, with 1 being a perfect score. The Probability of False Detection (POFD) is the ratio of misses against total negative results. POFD ranges from 0 to 1, with 0 being a perfect score. Along with the POD, these two ratios are accuracy measures of model discrimination. The False Alarm Ratio (FAR), also called False Positive Rate is the ratio between the number of negative events wrongly categorized as positive and the total number of actual negative events (false negatives + true negatives). The Miss Ratio (MR) is defined as the ratio between the number of misses and the sum of hits & misses, describing the conditional probability of a negative test result given that the condition being looked for is present. Both FAR and MR range from 0 to 1, with 0 being a perfect score. These two metrics are a measure of model reliability. The Threat Score (TS), also known as Critical Success Index is the ratio of all true positives against the sum of total number of occurrences and false alarms. Due to its neglect of non-occurrences, this score is well suited for scoring predictions of rare events like extreme driving during space weather events. The F_1 score, another measure of a test's accuracy, is defined as the harmonic mean of the POD and the hit rate, given by $(1-MR)$. Similar to the Threat Score, the F_1 score reaches its best value at 1 and worst at 0. The True Skill Score (TSS) or Hanssen-Kuiper Skill Score (Hanssen & Kuipers, 1965) is a performance metric with values ranging from -1 to +1, with 0 representing no skill. The TSS is defined as the difference between the hit rate (given by $1-MR$) and false alarm rate. Lastly, the Heidke Skill Score (HSS; Heidke, 1926) is a performance metric that measures the improvements in a model's results against random chance. Similarly to the TSS, the value of HSS ranges from -1 to +1, with 0 representing no skill. The HSS is popular in space weather forecasting, and has been established as a suitable comparative metric in several space weather studies (Welling & Ridley, 2010, *Pulkkinen2013*, Tóth et al., 2014, Welling et al., 2018).

3 Results & Discussion

3.1 Impact on Global Quantities

Figure 4 exhibits the variations in the pattern and magnitude of Hall conductance for simulations using the low-res *SWPC* configuration. Each dial-plot column displays the high latitude Hall conductance at different time instances from the simulation sets A, B, C and D respectively. The first row shows results from 04:33 UT on October 29, 2003 : toward the beginning of Event 1, before the sudden commencement with the storm index Kp less than 4. The second and third rows, titled Epoch 2 and Epoch 3, compare the four sets at 06:20 UT and 06:46 UT on the same day during the sudden commencement and main phase of Event 1, when $4 \leq Kp < 8$ and $Kp \geq 8$ respectively. As a reference, the bottom line plot shows the Kp throughout the event, along with the predicted Kp from the four simulation variants with the background coloured by the magnitude of Kp - green for $Kp < 4$, yellow for $4 \leq Kp < 8$, and red for $Kp \geq 8$.

Comparing results of Sets A and B, the increased dataset used in CMEE increases the max value of conductance and is capable of capturing auroral dynamics across different activity for every epoch. The addition of oval adjustments visibly alters the pattern of conductance - comparison of Sets A and B with their respective counterparts in

(a) List of Events

Event #	Date and Time
1	29 October 2003 06:00 UT - 30 October 06:00 UT
2	14 December 2006 12:00 UT - 16 December 00:00 UT
3	31 August 2001 00:00 UT - 1 September 00:00 UT
4	31 August 2005 10:00 UT - 1 September 12:00 UT
5	5 April 2010 00:00 UT - 6 April 00:00 UT
6	5 August 2011 09:00 UT - 6 August 09:00 UT

(b) List of SWMF Simulations

	<i>RLM Coeffs</i>	<i>CMEE Coeffs</i>	<i>RLM w OA</i>	<i>CMEE w OA</i>
SWPC	Set A	Set B	Set C	Set D
Hi-Res SWPC	Set E	Set F	Set G	Set H

RLM Coeffs - Empirical Coefficients of the Ridley Legacy Model
CMEE Coeffs - Empirical Coefficients of the Conductance Model for Extreme Events
RLM w OA - Ridley Legacy Model, with Auroral Oval Adjustments
CMEE w OA - Conductance Model for Extreme Events, with Auroral Oval Adjustments

Table 1. (a) List of space weather events used in this study to test and validate the different conductance models. This is the same set of events used in *Pulkkinen2013*. (b) A tabular description of all the simulations conducted for this study, binned by SWMF domain variations used: Each set of runs (denoted as 'SET ×', where × is the alphabetic value designated) is a simulation of all space weather events listed in (a), using a particular variation of the auroral conductance model (columns) within a given configuration of the SWMF (rows).

Performance Metric	Acronym	Mathematical Definition
Probability of Detection	POD	$\frac{TP}{(TP+FP)}$
Probability of False Detection	POFD	$\frac{FN}{(FN+TN)}$
False Alarm Ratio	FAR	$\frac{FP}{(FP+TN)}$
Miss Ratio	MR	$\frac{FN}{(TP+FN)}$
Threat Score	TS	$\frac{TP}{(TP+FN+FP)}$
F ₁ Score	F ₁	$\frac{2TP}{(2TP+FP+FN)}$
True Skill Score	TSS	$\frac{TP}{TP+FN} - \frac{FP+TN}{FP+TN} = (1 - MR) - FAR$
Heidke Skill Score	HSS	$\frac{2(TP \times TN - FP \times FN)}{((TP+FP)(FP+TN) + (TP+FN)(FN+TN))}$

Table 2. List of performance metrics used in this study.

414 Sets C & D illustrate how the adjustments intensify the conductance in regions of high
 415 field aligned currents, mimicking discrete arcs. The difference in Sets C & D, while not
 416 so apparent in Epochs 1 and 2, are substantially distinct in Epoch 3, when $Kp \geq 8$.
 417 In this case, the difference in the conductance caused by the combined usage of the in-
 418 creased dataset spanning extreme events and the additional oval-region enhancement re-
 419 sults in a higher conductance peak in Set D. For higher Kp , CMEE increases nightside
 420 conductance and lowers dayside conductance. This is because CMEE coefficients, a byprod-
 421 uct of an increased dataset spanning seasonal changes in addition to being estimated us-
 422 ing a nonlinear regression algorithm, computes lower dayside conductance and higher
 423 nightside conductance in comparison to the RLM coefficients. An unusual feature of us-
 424 ing FAC-directed empirical models is the emergence of islands of conductance during the
 425 peak of the storm (Epoch 3). These discontinuities are reduced by the initial usage of the
 426 smoothing function on the coefficients, and addition of a baseline value in the auroral
 427 oval region.

428 Figure 5 compares integrated field aligned currents (iFACs) observations during Event
 429 5 by AMPERE, against estimates from SWMF. Events 5 and 6 were observed by AM-
 430 PERE, and compared to models in Anderson et al. (2017). The iFACs were estimated
 431 similarly to Anderson et al. (2017) and were used to compare the effect of dataset ex-
 432 pansion in the top panel (a), the impact of oval adjustments in the middle panel (b), and
 433 the combined influence both in the bottom panel (c). In each of these panels, we com-
 434 pare the low resolution *SWPC* configuration of the SWMF simulations (Sets A, B, C
 435 and D) with the *Hi-Res SWPC* configuration simulations (Sets E, F, G and H) to vi-
 436 sualize the impact of conductance on the input conditions to IE. While minor variations
 437 are caused by the usage of different conductance models, no significant changes are ob-
 438 served either by using the CMEE coefficients or by adjusting the auroral oval. Instead,
 439 the results show the *Hi-Res SWPC* simulations being able to better capture the mag-
 440 nitude and dynamics of the iFACs than the *SWPC* configurations. This is in agreement
 441 with results from the study of Ridley et al. (2010) who investigated the impact of res-
 442 olution on ionospheric quantities like FACs, especially with respect to variation in val-
 443 ues as we change numerical resolution. While there are definite changes in the FACs and
 444 iFAC values due to the different auroral models, the increased resolution helps to cap-
 445 ture more of the FACs, dramatically improving the data-model comparison.

446 Figure 6 compares simulated cross polar cap potential (CPCP) for all simulation
 447 sets against values obtained from AMIE and SuperDARN, for Event 3, which was the
 448 only event in this study for which high quality AMIE and SuperDARN data were avail-
 449 able. Figure 6 is divided into three groups: in each group, the low res and high res sim-
 450 ulations are compared in separate subplots with the topmost group in part (a) illustrat-
 451 ing the impact of updated conductance coefficients on CPCP, middle group in part (b)
 452 investigating the impact of oval adjustments, and the bottom group in part (c) compar-
 453 ing the combined influence of dataset expansion and oval adjustments. The difference be-
 454 tween the AMIE CPCP, denoted by the solid black line, and SuperDARN CPCP, den-
 455 oted by the dot-dashed line, has been demarcated using a thick dark grey region in each
 456 subplot to give an envelope of expected values based on the observations-based estimates.

457 As shown in Figures 4 and 5, the introduction of CMEE and oval adjustments in-
 458 creases the value of the auroral conductance but does not dramatically impact the strength
 459 of FACs, for a given domain resolution. Since the electrostatic potential is the direct out-
 460 put of Ohm's Law, an increment in conductance with no substantial change in FACs leads
 461 to a lower value of CPCP. This is explicitly observed in part (a), where RLM-driven sim-
 462 ulations overestimates the CPCP in both the *SWPC* and *Hi-Res SWPC* cases, in com-
 463 parison to CMEE-driven simulations. The *Hi-Res* RLM case, denoted in yellow (Frame
 464 6a-ii), particularly stands out because the FAC-driven conductance reaches the ceiling
 465 set by the coefficient A_0 , i.e. as the magnitude of FACs increases, the value of conduc-
 466 tance attains the asymptotic maximum value (A_0) in the given model. Since the median

467 A_0 value is higher in CMEE it is able to give a reasonable CPCP estimate, while RLM's
 468 reduced conductance peaks during the strongest driving resulting in the CPCP being an
 469 order of magnitude greater. In part (b), conductance increments driven by oval adjust-
 470 ments largely reduces the CPCP, except during the main phase of the event when $Kp >$
 471 4. This is because, during peak driving, the conductance from both models is so large
 472 that the oval adjustments do not affect results substantially. In part (c), CMEE-driven
 473 CPCP is lower than RLM-driven CPCP, as is expected. The CPCP values from Set D
 474 (Frame 6c-i) are too low, indicating that the model is overestimating the conductance
 475 which resulted in a lower CPCP. For the *Hi-Res* case in Frame 6c-ii, the higher conduc-
 476 tance estimation coupled with better resolved FACs acts in favour of CMEE-driven sim-
 477 ulations in Set H, and leads to a more realistic CPCP as shown by the comparison against
 478 AMIE and SuperDARN. In all events, simulations driven with RLM tend to have a higher
 479 CPCP compared to CMEE, as the conductance ceiling is higher in CMEE than RLM.

480 Figure 7 illustrates the impact of conductance on dB/dt predictions during Event
 481 2, at two magnetometer stations - the high-latitude magnetometer station at Yellowknife
 482 (YKC) located at magnetic latitude (MLat) 68.93° N and magnetic longitude (MLon)
 483 299.36° , and the mid-latitude magnetometer station at Newport (NEW) located at MLat
 484 54.85° N and MLon 304.68° . While YKC and NEW are far apart latitudinally, longi-
 485 tudinally they are separated by less than 5° , making them a good candidate to study
 486 the expansion of the auroral oval under strong driving conditions. The background in
 487 each subplot, in addition to being coloured by Kp similar to Figures 5 and 6, are dark-
 488 ened to indicate times when the magnetometer was on the nightside. Additionally, dash-
 489 dot lines in all subplots indicate the four thresholds chosen in the *Pulkkinen2013* study.

490 Between 14:08 UT and 18:17 UT on December 14, 2006, as activity increases, mas-
 491 sive dB/dt spikes were observed at YKC with values crossing the four *Pulkkinen2013* thresh-
 492 olds. These spikes died down as activity increased, indicated by the increment in the Kp
 493 values. From \sim 18:20 UT to 07:04 UT on December 15, except for one massive spike at
 494 04:28 UT, dB/dt spikes at YKC barely cross the second and third threshold. During this
 495 time period, the magnetometer was mostly on the nightside. Interestingly, all substan-
 496 tial perturbations observed at NEW occur during this same time interval, between 22:21
 497 UT and 07:54 UT. This is an indication that the auroral oval expanded equatorward dur-
 498 ing this given time interval as shown by the auroral radiance measurements by Defence
 499 Meteorological Satellite Program (DMSP) F16 passes, with the storm intensifying. This
 500 expansion of the oval resulted in latitudinally-high YKC no longer being in the auroral
 501 zone and instead being in the polar cap region, while the lower boundaries of the auro-
 502 ral oval reached latitudinally-lower NEW. Starting at 07:54 UT, spikes at NEW died down
 503 and were almost negligible throughout the rest of the event. Around the same time, mas-
 504 sive spikes crossing all four thresholds were observed again at YKC as the magnetome-
 505 ter station approaches the midnight-dawn sector. The spikes at YKC were observed un-
 506 til 16:33 UT as the magnetometer station rotated to the dawn-noon sector, through the
 507 recovery period of the event.

508 In parts (b) and (c) of Figure 7, modeled dB/dt at YKC and NEW are compared
 509 against observations. The topmost panel in part (b) compares modeled dB/dt from Sets
 510 E and F addressing the impact of dataset expansion. The middle panel in (b) compares
 511 Sets F and H to address the effect of auroral oval adjustments, while the bottom panel
 512 compares Sets G and H to study the combined influence of both the expanded dataset
 513 and the oval adjustments. In part (c), modeled dB/dt from Sets G and H are compared
 514 against observations at NEW. To simplify visualization, the minute-resolution data from
 515 both observed and modeled dB/dt values in parts (b) and (c) have been max-filtered for
 516 every 10 minute interval. Additionally, the subplot background and threshold lines in
 517 parts (b) and (c) are plotted and coloured similarly to part (a).

518 In the top panel of part (b), the magnitude of the CMEE-simulated dB/dt spikes
 519 are mostly at par with or moderately larger than the RLM-simulated spikes through most

of the event. Both Sets E and F reasonably modeled the dB/dt during the time interval when the oval expanded and YKC was in the polar cap. However, they were unable to reproduce the heavy spikes that appeared both before and after the time interval, barely crossing the fourth threshold of 1.5 nT/s at any given instance. In the middle panel, both the frequency and magnitude of the dB/dt spikes increased significantly with the introduction of the oval adjustments. While this led to minor improvements in reproducing observations at time intervals when YKC observed heavy spikes, a substantial change occurred during the oval expansion when there were minimal dB/dt perturbations in both the observations and the coefficient-driven simulation results but intense spikes at high frequencies in the oval-adjusted simulation output. This increment in dB/dt spikes is dominant in the bottom panel of part (b) in both CMEE and RLM driven simulations. The impact of the dataset expansion combined with the oval adjustment in Set H simulations led to a sharp increase in the magnitude of the spikes, in addition to the sharp rise in frequency. Part (c) indicate that the model does not reproduce the dB/dt spikes at NEW, regardless of the conductance model used. This is in direct contrast to the results from the last panel of part (b) which compares the same model variants but shows multiple intense dB/dt spikes at YKC during the same time interval. This indicates that while usage of CMEE + oval adjustments improved the performance, there were still outstanding issues concerning the expansion and location of the oval that may require a more comprehensive, physics-based approach.

Figure 8 illustrates comparison magnetic perturbations ΔB at the same magnetometer stations during the same event to provide further clarity on the issue of auroral expansion. Part (a) compares the modeled and simulated ΔB at YKC and NEW during the event. At YKC, heavy fluctuations were observed in the ΔB values corresponding with the same time intervals when the massive spikes in dB/dt were observed in Figure 7(a): between 14:21 UT and 18:19 UT, on December 14, and 06:42 UT and 17:07 UT on December 15. The magnitude of ΔB were $\geq 500 \text{ nT}$ during these time intervals. At NEW, while all variations in ΔB were comparatively lower ($\leq 400 \text{ nT}$), heavy fluctuations were seen during the same time interval when the auroral oval expands and significant dB/dt perturbations in Figure 7(a) occur, between 23:37 UT and 12:07 UT. During the oval expansion phase, YKC-observed ΔB increases steadily with time producing minimal fluctuations during this period, retroactively indicating why the dB/dt is low.

In parts (b) and (c) of Figure 8, the simulated ΔB from Sets G and H reasonably reproduce the observed ΔB pattern. During the oval expansion phase of the event, the simulated ΔB of both sets fluctuate with higher frequency and magnitude than is observed at YKC, thereby explaining the massive spikes in the simulated dB/dt seen during the same time interval in Figure 7(b). Quantitatively, the Set H simulations exhibit the best performance with a symmetric signed bias percentage (SSPB; Morley et al., 2018) of $\sim 5.6\%$. Here, SSPB measures the symmetric bias in the forecast against the observed values. At NEW, comparison of the simulated ΔB from either sets do not differ substantially with each other, with a negligible difference of $\leq 1\%$ in their respective SSPB. Neither models are able to predict the perturbations during the main phase of the storm between 00:00 UT to 09:00 UT, explaining similarly poor performance in predicting the dB/dt values for this magnetometer. Part (d) compares the individual contributions of the global current systems - auroral Hall and Pedersen currents, field-aligned currents and magnetospheric currents, in the ΔB estimation at YKC and NEW from the Set H simulation. At YKC, auroral and field-aligned currents are the dominant current systems driving perturbations in the magnetic field while magnetospheric currents contribute negligibly. The opposite is true at NEW, where the ΔB variations are mostly driven by changes in the magnetospheric currents and field aligned currents, with auroral currents barely affecting the simulated ΔB even during the peak driving of the system, indicating minimal contribution. This is further corroborated by the dial plots in Part (e) with the top row showing the extent of saturated field aligned currents in the SWMF domain

574 and compares it to the domain boundary of the modeled auroral conductance in the bot-
575 tom row which clearly halts at 60 degree MLat.

576 The comparisons in Figures 7 and 8 indicate that in the modeled ΔB and dB/dt
577 values, the auroral currents have little or no impact on mid and low latitude magnetome-
578 ter predictions as the auroral oval is not able to extend equatorward to these latitudes.
579 While this is expected during quiet conditions, the impact of auroral currents during ex-
580 treme events can change dynamically with the expansion of the auroral oval, and can
581 extend to much lower latitudes as evidenced by NEW during this event. The impact of
582 this shortcoming on predictive skill has been described in further detail in Section 4.

583 3.2 Performance Quantification of dB/dt Comparisons

584 The results from the binary event analysis performed on the dB/dt predictions show
585 that changing the auroral conductance in the global model, either by expanding the dataset
586 or by applying the oval adjustments, led to minimal or no improvement in skill score for
587 the lowest dB/dt threshold, but improved skill for the remaining dB/dt thresholds, with
588 the most improvement in the highest thresholds. Table 3 presents a re-analysis of the
589 results from *Pulkkinen2013*, emphasizing the changes in the HSS of dB/dt results, that
590 were caused by CMEE and the auroral oval adjustments. In part (a) of the table, the
591 expansion of dataset results in the improvement of HSS in each threshold for both the
592 low and high resolution cases, as evidenced by the difference column. This addresses *Welling2017*'s
593 original question, that expansion of the dataset can lead to improvement in dB/dt pre-
594 dictions. In part (b), the HSS improvement caused by oval adjustments to the aurora
595 is more substantial than in part (a), with HSS going up by ~ 0.1 in the highest thresh-
596 olds for both *SWPC* and *Hi-Res SWPC* configurations. The comparison of both RLM
597 and CMEE combined with oval adjustments in case (c) show similar improvements in
598 predictive skill for the higher dB/dt thresholds when using CMEE with oval adjustments.

599 Figures 9(a) and (b) provide a quantitative picture of HSS improvement in the dB/dt
600 predictions over many more thresholds. In both subplots, the y -axis is HSS, while the
601 increasing dB/dt thresholds on the x -axis provide a quantitative value of space weather
602 activity. As expected, the HSS scores for all models decreased with increasing thresh-
603 old value. However, in the most-extreme thresholds CMEE-driven simulations out-perform
604 RLM-driven simulations, with improvements in the HSS of the same order as previously
605 evidenced in Table 3. The HSS values in the highest dB/dt thresholds for the low-resolution
606 runs of CMEE, in both parts (a) and (b), were either at par or larger than the HSS val-
607 ues for not only the low-resolution but also the high-resolution RLM simulations. This
608 is a significant improvement in the skill score due to CMEE, as this provides an alter-
609 nate physics-based remedy that otherwise could only be solved numerically. Naturally,
610 the HSS values of the high-resolution CMEE-driven simulations were the highest at al-
611 most all thresholds. Using this result, we can partially address the science questions posed
612 in Section 1 that the auroral conductance impacts the dB/dt significantly, and that im-
613 provements in the magnitude or pattern of the conductance boosts predictive skill scores
614 for strong driving of the system.

615 To better quantify the variation in model performance, the values of all performance
616 metrics listed in Table 2 were investigated. Table 4 presents these metrics calculated for
617 all model variants at the high dB/dt threshold of 1.5 nT/s. In this table, the results show
618 the *SWPC* configuration in the left and the *Hi-Res SWPC* configuration in the right,
619 with the worst performance by configuration coloured in orange and the best performance
620 coloured in blue. For both the *SWPC* and *Hi-Res SWPC* configurations, the POD and
621 MR improved quite significantly for CMEE and the oval adjustments, indicating that
622 the number of hits and misses increased and decreased, respectively. In addition, all skill
623 score metrics in the latter half of the table, excluding TSS, indicate best performance
624 for CMEE with oval adjustment variant for both resolutions of the model. The TS and

625 F_1 score increased indicating that the number of hits increased. As has been shown in
 626 the previous figure and table, the HSS improves as we switch models to introduce oval
 627 adjustments and expansion of the dataset. However, the opposite occurred when look-
 628 ing at POFD and FAR values were considered: the application of oval adjustments led
 629 to sharply increased FAR values in both low and high res configurations. While the hits
 630 and true negatives increased significantly and misses decreased, as supported by the POD
 631 and MR values, the number of false alarms increased steadily as the conductance coef-
 632 ficients were changed and jumped significantly with the application of the oval adjust-
 633 ments. This indirectly affected the TSS, which is defined as the difference between the
 634 hit rate and miss rate, or mathematically as $1 - (\text{FAR} + \text{MR})$. Since the FAR increased,
 635 in spite of the decreased MR, TSS values reduced by more than 0.05 as we switched mod-
 636 els. Given that this order of change in skill was similar to what was achievable by chang-
 637 ing model resolutions, the increment in false alarms is a significant drawback when us-
 638 ing oval adjustments. The aforementioned trend was observed in all dB/dt thresholds
 639 from 0.7 nT/s and above, indicating that this was not an isolated case. The performance
 640 metrics for the other thresholds have been presented in the supp. material.

641 3.3 Performance Analysis of ΔB Estimation

642 Unlike the dB/dt performance quantification using binary event analysis, the us-
 643 age of the same procedure on ΔB values does not help address the science questions posed
 644 in Section 1. Figure 10 describes variation in HSS for predicted ΔB from all model vari-
 645 ants against observed values. In comparison to the dB/dt predictions, the change in ΔB
 646 predictions were not nearly as drastic for better or worse. Note that the y-axis in Fig-
 647 ures 10(a) and (b) are not the same as in Figures 9(a) and (b); the HSS range spanned
 648 in the case of ΔB is much shorter than in the case of dB/dt . In part (a), the CMEE-
 649 driven predictions show deterioration in the HSS values compared to RLM. However, in
 650 comparison to the variation in HSS for dB/dt by the expanded dataset, the variation ob-
 651 served is minimal. The decrease in HSS values was similar, but lesser, in the *Hi-Res* Set
 652 F results. In part (b), the variation in ΔB HSS values are negligible when oval adjust-
 653 ments were applied, for both model resolutions. In fact, some higher thresholds in part
 654 (b) showed no substantial change in the HSS values with the CMEE-driven simulations.
 655 When comparing parts (a) and (b) of Figure 10, the HSS values in part (b) are greater
 656 than their respective counterpart in part (a) of the figure for thresholds ≥ 200 nT. This
 657 indicates that while changing coefficients by increasing the dataset caused more varia-
 658 tion in the HSS values of individual simulation sets, application of oval adjustments im-
 659 proves overall performance regardless of the coefficients used.

660 For a more quantitative explanation of the ΔB performance, Table 5 presents val-
 661 ues of all performance metrics calculated for all model variants at a high ΔB threshold
 662 of 400 nT. The table is similarly structured to Table 4 with the worst performance in
 663 each configuration coloured orange and the best performance coloured blue. When compar-
 664 ing the coefficient-driven simulations of RLM and CMEE, substantial variations are
 665 not observed in almost all skill scores with a maximum difference of ~ 0.02 for any given
 666 skill score and resolution. The same is seen with the simulations driven with oval adjust-
 667 ments, which also do not vary substantially. However, a significant jump is observed in
 668 the skill scores when comparing the impact of oval adjustments with oval adjusted sim-
 669 ulations performing better than only coefficient-driven simulations. For both low and
 670 high res configurations, TS and F_1 skill scores improve when oval adjustments are ap-
 671 plied. This is also seen in the accuracy measures like POD and MR whose values improve,
 672 with the POD jumping by a value of ~ 0.1 indicating that the number of hits are increas-
 673 ing and number of misses decreasing. Similar to the dB/dt metric analysis and in sharp
 674 contrast to the aforementioned performance metrics, the POFD and FAR values are best
 675 for simulations driven using non-oval adjustment applications. This is similar to the re-
 676 sults in Section 3.2, where false alarms increase as we switch conductance models. Sim-
 677 ilar to Section 3.2, the trend seen in these performance metrics are not an isolated case

(a) Impact of Dataset Expansion

Threshold	SWPC Configuration			Hi-Res SWPC Configuration		
	RLM	CMEE	Difference	RLM	CMEE	Difference
0.3 nT/s	0.521	0.554	+0.033	0.624	0.640	+0.016
0.7 nT/s	0.445	0.478	+0.033	0.526	0.559	+0.033
1.1 nT/s	0.353	0.394	+0.040	0.434	0.466	+0.032
1.5 nT/s	0.285	0.312	+0.027	0.330	0.367	+0.037

(b) Effect of Oval Adjustment (OA)

Threshold	SWPC Configuration			Hi-Res SWPC Configuration		
	CMEE	CMEE ⁺	Difference	CMEE	CMEE ⁺	Difference
0.3 nT/s	0.554	0.637	+0.083	0.640	0.685	+0.046
0.7 nT/s	0.478	0.556	+0.078	0.559	0.619	+0.060
1.1 nT/s	0.394	0.474	+0.080	0.466	0.525	+0.059
1.5 nT/s	0.312	0.397	+0.085	0.367	0.465	+0.098

(c) Influence of Dataset expansion and OA Combination

Threshold	SWPC Configuration			Hi-Res SWPC Configuration		
	RLM ⁺	CMEE ⁺	Difference	RLM ⁺	CMEE ⁺	Difference
0.3 nT/s	0.637	0.637	±0.000	0.699	0.685	-0.013
0.7 nT/s	0.498	0.556	+0.058	0.598	0.619	+0.022
1.1 nT/s	0.406	0.474	+0.068	0.492	0.525	+0.033
1.5 nT/s	0.318	0.397	+0.079	0.409	0.465	+0.056

RLM - Empirical Coefficients of the Ridley Legacy Model
 CMEE - Empirical Coefficients of the Conductance Model for Extreme Events
 RLM⁺ - Ridley Legacy Model, with Auroral Oval Adjustments
 CMEE⁺ - Conductance Model for Extreme Events, with Auroral Oval Adjustments

Table 3. Comparison of Heidke Skill Scores (HSS) for the space weather events listed in Table 1(a) at the prescribed four dB/dt thresholds (leftmost column) from *Pulkkinen2013*. (a) The top-most table compares HSS for the conductance coefficients of RLM and CMEE; no auroral amelioration added to the model; (b) The middle table compares results simulated using the CMEE using only the empirical conductance coefficients, against another version of the model that uses the CMEE coefficients along with the artificial oval adjustments; (c) The bottom-most table compares the two empirical models with the auroral oval adjustments. Here, green signifies improvement, while red signifies deterioration in prediction value.

678 for this specific threshold, but observed in all thresholds. The performance metrics for
 679 the other thresholds have been presented in the supp. material.

680 The TSS and HSS do not show substantial differences as the conductance is mod-
 681 ified, with the maximum difference between skill scores not being more than ~ 0.05 . By
 682 comparison, the difference between the best and the worst HSS performance for the dB/dt
 683 is ~ 0.11 . The results also show that the best HSS and TSS for the *Hi-Res* case are sim-
 684 ulations driven by RLM coefficients, which is in direct contrast to the low res case where
 685 RLM coefficients consistently underperform for both TSS and HSS. This contrast is as
 686 a result of using the same time forecast window t_f as the *Pulkkinen2013* on ΔB predic-
 687 tions. The comparison window t_f of 20 minutes, used in both this study and the *Pulkki-*
 688 *nen2013* study for dB/dt predictions, is not long enough to observe severe variations in

689 ΔB perturbations. As an example, the predicted ΔB hardly varies over more than two
 690 of the pre-determined thresholds, even during strong driving. In comparison, dB/dt varies
 691 over multiple thresholds several times within a t_f . This shows that the metrics used in
 692 this study are not totally appropriate to study improvements in ΔB predictions. This
 693 could simply be done by increasing the comparison time window, or by using different
 694 error or bias metrics. As discussed earlier in Section 3.1 estimation of SSPB in Figure
 695 8 for specific magnetometer stations during Event 2 gives a quantitative understanding
 696 of the difference.

697 4 Analysis

698 The considerable increase in the frequency and magnitude of dB/dt spikes at YKC
 699 with the application of the oval adjustments in Figure 7(b) is closely associated to the
 700 domain constraints in RIM. As described in Section 2.2.1, while RIM's simulation do-
 701 main spans the ionosphere pole-to-pole, the empirical auroral conductance module is lim-
 702 ited with a spatial domain spanning the poles to MLat 60° . This means that in its present
 703 configuration the auroral conductance module, be it RLM or CMEE, is bounded at MLat
 704 60° , with conductance values equatorward of this boundary dropping exponentially and
 705 the aurora being constrained poleward of the boundary. The impact of this boundary
 706 is clearly indicated in Figure 8(d), where auroral currents are the dominant source of ground
 707 ΔB in high latitude regions like YKC, but contribute negligibly at mid latitudinal re-
 708 gions like NEW.

709 Since application of both the dataset expansion and oval adjustments result in in-
 710 creasing the conductance ceiling during strong driving, CMEE allows more magnetospheric
 711 currents to close more dynamically throughout the ionosphere at any given time. In ad-
 712 dition, the oval adjustments enhance conductance in regions of high upward FACs thereby
 713 changing the pattern of the auroral conductance and reducing the conductance as a func-
 714 tion of distance from the empirically constructed oval. The combined effect of these mod-
 715 ifications would result in the auroral horizontal currents in RIM's domain being estimated
 716 with increased accuracy. This, in turn, leads to a more accurate estimation of the ΔB
 717 perturbation and subsequently dB/dt , which are both calculated from the Biot-Savart
 718 integral of these current systems (e.g. Yu et al., 2010; Welling, 2019). The conductance
 719 modifications due to the two elements (dataset expansion and oval adjustment) lead to
 720 noisier results in dB/dt , which leads to increased spikes. These spikes, when correct, in-
 721 crease the number of hits and when incorrect, increase the number of false alarms. The
 722 emergence of dB/dt spikes in the modeled data during the oval expansion phase in the
 723 bottom subplot of Figure 7(b) demarcates why false alarms increase when the oval ad-
 724 justment factor is used. In addition to the boundary constraints, false alarms are also
 725 caused by sudden shifting of the empirically-estimated auroral oval. These shifts are caused
 726 as a result of the sensitive dependence of the oval adjustments to changes in FAC pat-
 727 terns. Sharp changes in the FAC occurring over time scales in the same order of the cou-
 728 pling time cadence cause the empirical estimation of the oval to change rapidly. This brisk
 729 movement of the placement of the oval adjustment results in the loci movement of dB/dt
 730 spikes, causing unexpected hits and/or false alarms. In all, the aforementioned problems
 731 place the auroral oval in the wrong spot which lead to dB/dt spikes, perhaps even at the
 732 right time, but wrong location hence increasing the false alarms.

733 While an increment in the number of false alarms is a significant drawback, the ad-
 734 vantages of using the improved conductance model in the SWMF far outweigh this is-
 735 sue. Firstly, the expansion of the dataset in CMEE allows for an increased limit cap on
 736 the magnitude of the conductance which results in generating a more realistic cross pol-
 737 ar cap potential to be fed back as input to the GM and IM modules. This is essential
 738 when conducting numerical experiments investigating the magnetosphere-ionosphere cou-
 739 pling. Secondly, the changes in the conductance pattern in CMEE, as a result of the use
 740 of nonlinear regression, physically alters the nightside and dayside auroral conductance

Metric	<i>SWPC</i> Configuration				<i>Hi-Res SWPC</i> Configuration			
	RLM	CMEE	RLM ⁺	CMEE ⁺	RLM	CMEE	RLM ⁺	CMEE ⁺
POD	0.2216	0.2490	0.2668	0.3557	0.2791	0.3406	0.4309	0.5554
POFD	0.0169	0.0194	0.0253	0.0319	0.0262	0.0378	0.0566	0.0784
FAR	0.3306	0.3358	0.3810	0.3674	0.3780	0.4182	0.4597	0.4775
MR	0.1089	0.1057	0.1041	0.0932	0.1026	0.0957	0.0852	0.0693
TS	0.1998	0.2211	0.2291	0.2948	0.2386	0.2736	0.3153	0.3684
F1	0.3330	0.3622	0.3728	0.4553	0.3853	0.4297	0.4795	0.5385
TSS	0.5605	0.5585	0.5150	0.5394	0.5194	0.4861	0.4551	0.4532
HSS	0.2855	0.3120	0.3179	0.3973	0.3297	0.3672	0.4094	0.4647

Table 4. Performance metrics table for predicted dB/dt at the $1.5 nT/s$ threshold. Listed are all performance metrics defined in Table 2 (Leftmost column) measured for SWMF simulations conducted using RLM Coefficients (denoted by 'RLM'), CMEE Coefficients (denoted by 'CMEE'), RLM with oval adjustment (denoted by 'RLM⁺') and CMEE with oval adjustment (denoted by 'CMEE⁺') simulated using both the *SWPC* and *Hi-Res SWPC* configurations. The orange values show the least desirable metric results, while the blue values signify the best results for this threshold.

Metric	<i>SWPC</i> Configuration				<i>Hi-Res SWPC</i> Configuration			
	RLM	CMEE	RLM ⁺	CMEE ⁺	RLM	CMEE	RLM ⁺	CMEE ⁺
POD	0.4602	0.4385	0.5123	0.5224	0.5687	0.5485	0.6440	0.6671
POFD	0.0575	0.0523	0.0616	0.0658	0.0865	0.0901	0.1393	0.1429
FAR	0.2587	0.2500	0.2516	0.2602	0.2982	0.3146	0.3768	0.3745
MR	0.1701	0.1749	0.1568	0.1546	0.1445	0.1508	0.1289	0.1220
TS	0.3965	0.3826	0.4370	0.4413	0.4580	0.4382	0.4635	0.4767
F1	0.5679	0.5534	0.6082	0.6124	0.6283	0.6093	0.6335	0.6457
TSS	0.5712	0.5751	0.5916	0.5851	0.5573	0.5346	0.4943	0.5035
HSS	0.4585	0.4456	0.5015	0.5042	0.5135	0.4898	0.4994	0.5132

Table 5. Performance metrics table for predicted ΔB at the $400 nT$ threshold. Listed are all performance metrics defined in Table 2 (Leftmost column) measured for SWMF simulations conducted using the same variants as in Table 4. The orange values show the least desirable metric results, while the blue values signify the best results for this threshold.

741 pattern when compared to RLM. Using global modeling, this numerical experiment has
742 not only been able to address the question of expanded dataset raised by *Welling2017*,
743 but is also able to discern the impact of ionospheric conductance on space weather fore-
744 casting. Finally, both the magnitude and pattern of ionospheric conductance proves to
745 be an important quantity in affecting a global model's dB/dt predictive skill. Given that
746 the dB/dt is an important quantity used in the science community and the industry to
747 predict space weather on the ground, accuracy in the ionospheric conductance is impor-
748 tant in our global models. Through this work, the authors present an advanced and more
749 accurate auroral conductance model to address this challenge.

750 5 Conclusion

751 In this work, the development of an advanced auroral conductance model, CMEE
752 has been presented. CMEE has been designed using nonlinear regression to span minute-

753 resolution data generated from AMIE for the whole year of 2003 spanning extreme events.
754 It has additional capability to add physics-driven empirical adjustments to improve the
755 auroral conductance to ensure a larger range on conductance values to better predict the
756 conductance for a broad range of activity. In this study, this model has been used in the
757 SWMF to investigate the impact of auroral conductance on space weather prediction.
758 Simulated results were compared against observed global quantities like polar cap po-
759 tential, field aligned current intensity and ground-based magnetic perturbation. Addi-
760 tionally, a quantitative investigation was conducted using a binary event analysis simi-
761 lar to the *Pulkkinen2013* study and skill scores for dB/dt and ΔB predictions were com-
762 puted.

763 The investigation showed that application of the increased dataset coupled with
764 oval adjustments led to substantial changes in almost all space weather quantities. CMEE
765 allows the auroral conductance to have an increased range of values, attaining a higher
766 ceiling during extreme driving as compared to RLM. Since FACs are largely driven by
767 upstream conditions, they were not drastically impacted by changes in the conductance
768 model. However, since the conductance value increased and FACs varied minimally, the
769 CPCP values were lowered with the usage of CMEE and the oval adjustments. Since,
770 auroral horizontal currents directly impact the ground magnetic perturbation ΔB and
771 its temporal variant dB/dt , the driving of both these quantities were appreciably altered
772 by the application of both the expanded dataset and oval adjustments. While usage of
773 the expanded dataset resulted in a general increase of the modeled dB/dt magnitude,
774 oval adjustments increased the frequency of dB/dt spikes. Neither of these properties
775 were able to improve the modeling of the auroral oval expansion. This resulted in the
776 formation of different regimes in the latitudinal contribution to the ΔB and dB/dt dis-
777 tributions, with negligible contribution of auroral currents in low or mid latitude mag-
778 netometer stations in the modeled output during extreme driving.

779 The results of the binary event analysis conducted on the simulation variants indi-
780 cated that usage of CMEE with oval adjustments yields best performance, with dras-
781 tic improvements in the HSS metric at higher activity thresholds. In addition, most per-
782 formance metrics exhibited favourable changes when applying the CMEE coefficients and/or
783 oval adjustments, indicating an increase in the number of identified hits and true neg-
784 atives and a decrease in misses. However, the performance metrics also indicated that
785 the number of false alarms increased with the application of the oval adjustment. This
786 was caused predominantly because of the brisk movement of the empirically-estimated
787 oval, and the latitudinal constraint on the auroral conductance which inhibits the oval
788 from expanding beyond MLat 60° , thereby pushing the auroral currents poleward. While
789 this process increases the number of hits, favourably affecting most performance met-
790 rics, it also hurts metrics like TSS due to increased number of false alarms. The binary
791 event analysis of ΔB predictions do not yield definitive results, exhibiting minimal im-
792 pact on skill scores. This is most likely because the time forecast window of 20 minutes,
793 chosen to study dB/dt forecasts in the original *Pulkkinen2013* study, is limited for the
794 ΔB to exhibit significant change in value so as to jump multiple number of thresholds
795 and therefore produce any meaningful changes in the performance metrics. Outstand-
796 ing shortcomings of the present analysis such as those mentioned above and additional
797 analysis like estimation of bias and error metrics for various thresholds are steps that
798 we are presently pursuing. In addition, a key drawback of the present approach is neg-
799 ligence of the accuracy in AMIE's conductance estimation process during times of ex-
800 treme driving, since AMIE also derives the auroral conductance using an empirical re-
801 lationship (Ahn et al., 1998). Because validation is a process, continued data-model com-
802 parisons will be performed in future studies. Further comparisons of the conductance
803 estimates, field aligned current and potential patterns against measurements by AMIE,
804 SuperDARN and DMSP crossings will be presented.

805 The issues causing the misidentification of dB/dt spikes requires a physical solu-
 806 tion with numerical modifications to allow the aurora to expand to mid or low latitudes
 807 during extreme events. While this could be done with data, an easier and more novel
 808 solution would be to drive precipitation from the magnetospheric domains. This could
 809 be done by coupling physics-based precipitative inputs from GM and IM modules to es-
 810 timate electron and ion precipitation in the aurora. This is similar to what has been done
 811 in studies like Raeder et al. (2001) and Wiltberger et al. (2001). Such an approach al-
 812 lows for a novel approach to isolate and understand the impact of individual sources of
 813 auroral conductance. At the same time, the precipitation pattern of the aurora allows
 814 observational data from extreme events to feature prominently in perceiving the accu-
 815 racy of precipitative fluxes at different MLTs and magnetic latitudes. The development
 816 of such a model is presently being undertaken by the authors to address the aforemen-
 817 tioned issues of dataset inconsistencies and oval expansion (Mukhopadhyay et al., 2018,
 818 2019).

819 In conclusion, the usage of CMEE designed using an increased dataset coupled with
 820 the application of oval adjustment parameters lead to substantial changes in our dB/dt
 821 predictions. With the crucial impact that the auroral conductance imparts on global quan-
 822 tities, CMEE would serve as a competent replacement to RLM's coefficient map. The
 823 usage of the oval adjustments in the SWMF's auroral conductance estimation is unique
 824 and compelling in driving future developments of auroral conductance models to acheive
 825 accuracy in the conductance pattern, in addition to the magnitude. Additionally, as ev-
 826 idenced by the skill score analysis, the new model leads to significant improvement in
 827 predictive skill of our space weather model.

828 Acknowledgments

829 Support for this work has been provided by NASA Grants NNX17AB87G, 80NSSC18K1120,
 830 and 80NSSC17K0015, and NSF Grant 1663770. We would like to acknowledge high-performance
 831 computing support from Pleiades (allocation 1815) provided by NASA's High-End Com-
 832 puting Capability Programme, and Cheyenne (allocation UUSL0016) provided by NCAR's
 833 Computational and Information Systems Laboratory, sponsored by the National Science
 834 Foundation. Model result data, input files and observation data are available via [https://doi.org/10.7302/nwxp-](https://doi.org/10.7302/nwxp-g551)
 835 [g551](https://doi.org/10.7302/nwxp-g551). The Space Weather Modeling Framework is maintained by the University of Michi-
 836 gan Center for Space Environment Modeling and can be obtained at <http://csem.engin.umich.edu/tools/swmf>.
 837 AMIE Results used in this study are maintained at the University of Michigan's Virtual
 838 Model Repository (VMR; <http://vmr.engin.umich.edu/>). The authors thank NASA Com-
 839 munity Coordinated Modeling Center (CCMC) Staff and INTERMAGNET (<https://intermagnet.github.io/>)
 840 for providing the magnetometer measurements. The authors would also like to thank the
 841 Geomagnetism Unit of the Geological Survey of Canada (GSC) and the United States
 842 Geological Survey (USGS); Jeffrey J. Love for maintaining magnetometer measurements
 843 at Yellowknife and Newport respectively for public usage.

844 The authors would like to thank Dr. Meghan Burleigh for reading a draft manuscript.
 845 We thank Dr. Shasha Zou, Dr. Robert Robinson, Dr. Steven Morley and Dr. Gabor Toth
 846 for sharing their expertise in the course of this study. A.M. would like to thank Dr. Do-
 847 gacan su Ozturk, Dr. Zhenguang Huang, Dr. Natalia Ganjushkina, Ms. Abigail Azari,
 848 Mr. Alexander Shane, Mr. Brian Swiger and Mr. Christopher Bert for sharing their ex-
 849 pertise during the development of modeling, curve-fitting and validation tools used in
 850 this study.

851 References

852 Ahn, B.-H., Richmond, A. D., Kamide, Y., Kroehl, H. W., Emery, B. A., de la
 853 Beaujardi re, O., & Akasofu, S.-I. (1998, jul). An ionospheric conduc-
 854 tance model based on ground magnetic disturbance data. *Journal of Geo-*

- 855 *physical Research: Space Physics*, 103(A7), 14769–14780. Retrieved from
 856 <http://doi.wiley.com/10.1029/97JA03088> doi: 10.1029/97JA03088
- 857 Anderson, B. J., Korth, H., Waters, C. L., Green, D. L., Merkin, V. G., Barnes,
 858 R. J., & Dyrud, L. P. (2014). Development of large-scale birkeland currents de-
 859 termined from the active magnetosphere and planetary electrodynamics response
 860 experiment. *Geophysical Research Letters*, 41(9), 3017–3025. Retrieved from
 861 <https://agupubs.onlinelibrary.wiley.com/doi/abs/10.1002/2014GL059941>
 862 doi: 10.1002/2014GL059941
- 863 Anderson, B. J., Korth, H., Welling, D. T., Merkin, V. G., Wiltberger, M. J.,
 864 Raeder, J., ... Rastaetter, L. (2017). Comparison of predictive estimates of
 865 high-latitude electrodynamics with observations of global-scale birkeland currents.
 866 *Space Weather*, 15(2), 352–373. Retrieved from [https://agupubs.onlinelibrary](https://agupubs.onlinelibrary.wiley.com/doi/abs/10.1002/2016SW001529)
 867 [.wiley.com/doi/abs/10.1002/2016SW001529](https://agupubs.onlinelibrary.wiley.com/doi/abs/10.1002/2016SW001529) doi: 10.1002/2016SW001529
- 868 Axford, W. I., & Hines, C. O. (1961). A Unifying Theory of High-Latitude Geophys-
 869 ical Phenomena and Geomagnetic Storms. *Canadian Journal of Physics*, 39(10),
 870 1433–1464. Retrieved from <https://doi.org/10.1139/p61-172> doi: 10.1139/
 871 p61-172
- 872 Boonsiriseth, A., Thorne, R. M., Lu, G., Jordanova, V. K., Thomsen, M. F., Ober,
 873 D. M., & Ridley, A. J. (2001, jul). A semiempirical equatorial mapping of
 874 AMIE convection electric potentials (MACEP) for the January 10, 1997, mag-
 875 netic storm. *Journal of Geophysical Research: Space Physics*, 106(A7), 12903–
 876 12917. Retrieved from <http://doi.wiley.com/10.1029/1999JA000332> doi:
 877 10.1029/1999JA000332
- 878 Brekke, A., & Moen, J. (1993). Observations of high latitude ionospheric con-
 879 ductances. *Journal of Atmospheric and Terrestrial Physics*, 55(11), 1493–
 880 1512. Retrieved from [http://www.sciencedirect.com/science/article/](http://www.sciencedirect.com/science/article/pii/002191699390126J)
 881 [pii/002191699390126J](http://www.sciencedirect.com/science/article/pii/002191699390126J) doi: [https://doi.org/10.1016/0021-9169\(93\)90126-J](https://doi.org/10.1016/0021-9169(93)90126-J)
- 882 Carter, J. A., Milan, S. E., Coxon, J. C., Walach, M.-T., & Anderson, B. J. (2016).
 883 Average field-aligned current configuration parameterized by solar wind con-
 884 ditions. *Journal of Geophysical Research: Space Physics*, 121(2), 1294–1307.
 885 Retrieved from [https://agupubs.onlinelibrary.wiley.com/doi/abs/10.1002/](https://agupubs.onlinelibrary.wiley.com/doi/abs/10.1002/2015JA021567)
 886 [2015JA021567](https://agupubs.onlinelibrary.wiley.com/doi/abs/10.1002/2015JA021567) doi: 10.1002/2015JA021567
- 887 Chapman, S. (1931, jan). The absorption and dissociative or ionizing effect of
 888 monochromatic radiation in an atmosphere on a rotating earth. *Proceedings of*
 889 *the Physical Society*, 43(1), 26–45. Retrieved from [http://stacks.iop.org/](http://stacks.iop.org/0959-5309/43/i=1/a=305?key=crossref.46895a3aef390982dcfb99f7afc88ced)
 890 [0959-5309/43/i=1/a=305?key=crossref.46895a3aef390982dcfb99f7afc88ced](http://stacks.iop.org/0959-5309/43/i=1/a=305?key=crossref.46895a3aef390982dcfb99f7afc88ced)
 891 doi: 10.1088/0959-5309/43/1/305
- 892 Cid, C., Saiz, E., Guerrero, A., Palacios, J., & Cerrato, Y. (2015). A Carrington-like
 893 geomagnetic storm observed in the 21st century. *J. Space Weather Space Clim.*, 5,
 894 A16. Retrieved from <https://doi.org/10.1051/swsc/2015017> doi: 10.1051/
 895 swsc/2015017
- 896 Connor, H. K., Zesta, E., Fedrizzi, M., Shi, Y., Raeder, J., Codrescu, M. V., &
 897 Fuller-Rowell, T. J. (2016). Modeling the ionosphere-thermosphere response
 898 to a geomagnetic storm using physics-based magnetospheric energy input:
 899 OpenGGCM-CTIM results. *Journal of Space Weather and Space Climate*, 6,
 900 A25. Retrieved from <http://www.swsc-journal.org/10.1051/swsc/2016019>
 901 doi: 10.1051/swsc/2016019
- 902 De Zeeuw, D. L., Sazykin, S., Wolf, R. A., Gombosi, T. I., Ridley, A. J., & Tóth,
 903 G. (2004). Coupling of a global MHD code and an inner magnetospheric model:
 904 Initial results. *Journal of Geophysical Research: Space Physics*, 109(A12), 1–14.
 905 doi: 10.1029/2003JA010366
- 906 Doherty, P., Coster, A. J., & Murtagh, W. (2004). Space weather effects of Octo-
 907 ber–November 2003. *GPS Solutions*, 8(4), 267–271. Retrieved from [https://doi](https://doi.org/10.1007/s10291-004-0109-3)
 908 [.org/10.1007/s10291-004-0109-3](https://doi.org/10.1007/s10291-004-0109-3) doi: 10.1007/s10291-004-0109-3

- 909 Dungey, J. W. (1963, jan). Interactions of solar plasma with the geomag-
 910 netic field. *Planetary and Space Science*, *10*, 233–237. Retrieved from
 911 <https://www.sciencedirect.com/science/article/pii/0032063363900205>
 912 doi: 10.1016/0032-0633(63)90020-5
- 913 Frahm, R. A., Winningham, J. D., Sharber, J. R., Link, R., Crowley, G., Gaines,
 914 E. E., ... Potemra, T. A. (1997, dec). The diffuse aurora: A significant source
 915 of ionization in the middle atmosphere. *Journal of Geophysical Research: At-*
 916 *mospheres*, *102*(D23), 28203–28214. Retrieved from [http://doi.wiley.com/](http://doi.wiley.com/10.1029/97JD02430)
 917 [10.1029/97JD02430](http://doi.wiley.com/10.1029/97JD02430) doi: 10.1029/97JD02430
- 918 Fuller-Rowell, T. J., & Evans, D. S. (1987). Height-integrated pedersen and hall
 919 conductivity patterns inferred from the tiros-noaa satellite data. *Journal of Geo-*
 920 *physical Research: Space Physics*, *92*(A7), 7606–7618. Retrieved from [https://](https://agupubs.onlinelibrary.wiley.com/doi/abs/10.1029/JA092iA07p07606)
 921 agupubs.onlinelibrary.wiley.com/doi/abs/10.1029/JA092iA07p07606 doi:
 922 [10.1029/JA092iA07p07606](https://doi.org/10.1029/JA092iA07p07606)
- 923 Gao, Y. (2012). Comparing the cross polar cap potentials measured by superdarn
 924 and amie during saturation intervals. *Journal of Geophysical Research: Space*
 925 *Physics*, *117*(A8). Retrieved from [https://agupubs.onlinelibrary.wiley.com/](https://agupubs.onlinelibrary.wiley.com/doi/abs/10.1029/2012JA017690)
 926 [doi/abs/10.1029/2012JA017690](https://agupubs.onlinelibrary.wiley.com/doi/abs/10.1029/2012JA017690) doi: 10.1029/2012JA017690
- 927 Glocer, A., Rastätter, L., Kuznetsova, M., Pulkkinen, A., Singer, H. J., Balch, C.,
 928 ... Wing, S. (2016). Community-wide validation of geospace model local k-index
 929 predictions to support model transition to operations. *Space Weather*, *14*(7),
 930 469–480. Retrieved from [https://agupubs.onlinelibrary.wiley.com/doi/abs/](https://agupubs.onlinelibrary.wiley.com/doi/abs/10.1002/2016SW001387)
 931 [10.1002/2016SW001387](https://agupubs.onlinelibrary.wiley.com/doi/abs/10.1002/2016SW001387) doi: 10.1002/2016SW001387
- 932 Gombosi, T. I., De Zeeuw, D. L., Powell, K. G., Ridley, A. J., Sokolov, I. V., Stout,
 933 Q. F., & Tóth, G. (2003). Adaptive mesh refinement for global magnetohy-
 934 drodynamic simulation. In J. Büchner, M. Scholer, & C. T. Dum (Eds.), *Space*
 935 *plasma simulation* (pp. 247–274). Berlin, Heidelberg: Springer Berlin Heidel-
 936 berg. Retrieved from https://doi.org/10.1007/3-540-36530-3_12 doi:
 937 [10.1007/3-540-36530-3_12](https://doi.org/10.1007/3-540-36530-3_12)
- 938 Goodman, M. L. (1995, aug). A three-dimensional, iterative mapping procedure
 939 for the implementation of an ionosphere-magnetosphere anisotropic Ohm’s law
 940 boundary condition in global magnetohydrodynamic simulations. *Annales*
 941 *Geophysicae*, *13*(8), 843–853. Retrieved from [https://doi.org/10.1007/](https://doi.org/10.1007/s00585-995-0843-z)
 942 [s00585-995-0843-z](https://doi.org/10.1007/s00585-995-0843-z) doi: 10.1007/s00585-995-0843-z
- 943 Haiducek, J. D., Welling, D. T., Ganushkina, N. Y., Morley, S. K., & Ozturk, D. S.
 944 (2017). SWMF Global Magnetosphere Simulations of January 2005: Geomagnetic
 945 Indices and Cross-Polar Cap Potential. *Space Weather*, *15*(12), 1567–1587. Re-
 946 trieved from [https://agupubs.onlinelibrary.wiley.com/doi/abs/10.1002/](https://agupubs.onlinelibrary.wiley.com/doi/abs/10.1002/2017SW001695)
 947 [2017SW001695](https://agupubs.onlinelibrary.wiley.com/doi/abs/10.1002/2017SW001695) doi: 10.1002/2017SW001695
- 948 Hanssen, A. W., & Kuipers, W. J. A. (1965). On the relationship between the fre-
 949 quency of rain and various meteorological parameters. *Meded. Verh.*, *81*, 2 – 15.
- 950 Hartinger, M. D., Xu, Z., Clauer, C. R., Yu, Y., Weimer, D. R., Kim, H., ... Willer,
 951 A. N. (2017). Associating ground magnetometer observations with current or
 952 voltage generators. *Journal of Geophysical Research: Space Physics*, *122*(7), 7130-
 953 7141. Retrieved from [https://agupubs.onlinelibrary.wiley.com/doi/abs/](https://agupubs.onlinelibrary.wiley.com/doi/abs/10.1002/2017JA024140)
 954 [10.1002/2017JA024140](https://agupubs.onlinelibrary.wiley.com/doi/abs/10.1002/2017JA024140) doi: 10.1002/2017JA024140
- 955 Heidke, P. (1926). Berechnung des Erfolges und der Güte der
 956 Windstärkevorhersagen im Sturmwarnungsdienst. *Geografiska Annaler*, *8*, 301–
 957 349.
- 958 Herrmann, L. R. (1976). Laplacian-Isoparametric Grid Generation Scheme. *Journal*
 959 *of the Engineering Mechanics Division*, *102*(5), 749–907.
- 960 Honkonen, I., Rastätter, L., Grocott, A., Pulkkinen, A., Palmroth, M., Raeder,
 961 J., ... Wiltberger, M. (2013, may). On the performance of global magneto-
 962 hydrodynamic models in the Earth’s magnetosphere. *Space Weather*, *11*(5),

- 313–326. Retrieved from <http://doi.wiley.com/10.1002/swe.20055> doi:
10.1002/swe.20055
- Iijima, T., & Potemra, T. A. (1976). The amplitude distribution of field-aligned currents at northern high latitudes observed by Triad. *Journal of Geophysical Research-Space Physics*, *81*(13), 2165–2174. Retrieved from <http://onlinelibrary.wiley.com/doi/10.1029/JA081i013p02165/abstract> doi: 10.1029/JA081i013p02165
- Jolliffe, I. T., & Stephenson, D. B. (2012). *Forecast Verification: A Practitioner's Guide in Atmospheric Science*. John Wiley & Sons. Retrieved from <https://books.google.com/books?hl=en&lr=&id=DCxsKQeaBH8C&pgis=1>
- Kaeppler, S. R., Hampton, D. L., Nicolls, M. J., Strømme, A., Solomon, S. C., Hecht, J. H., & Conde, M. G. (2015). An investigation comparing ground-based techniques that quantify auroral electron flux and conductance. *Journal of Geophysical Research: Space Physics*, *120*(10), 9038–9056. Retrieved from <https://agupubs.onlinelibrary.wiley.com/doi/abs/10.1002/2015JA021396> doi: 10.1002/2015JA021396
- Khachikjan, G. Y., Koustov, A. V., & Sofko, G. J. (2008). Dependence of superdarn cross polar cap potential upon the solar wind electric field and magnetopause subsolar distance. *Journal of Geophysical Research: Space Physics*, *113*(A9). Retrieved from <https://agupubs.onlinelibrary.wiley.com/doi/abs/10.1029/2008JA013107> doi: 10.1029/2008JA013107
- Kihn, E. A., & Ridley, A. J. (2005). A statistical analysis of the assimilative mapping of ionospheric electrodynamic auroral specification. *Journal of Geophysical Research: Space Physics*, *110*(A7). Retrieved from <https://agupubs.onlinelibrary.wiley.com/doi/abs/10.1029/2003JA010371> doi: 10.1029/2003JA010371
- Knight, S. (1973). Parallel electric fields. *Planetary and Space Science*. doi: 10.1016/0032-0633(73)90093-7
- Korth, H., Zhang, Y., Anderson, B. J., Sotirelis, T., & Waters, C. L. (2014). Statistical relationship between large-scale upward field-aligned currents and electron precipitation. *Journal of Geophysical Research: Space Physics*, *119*(8), 6715–6731. Retrieved from <https://agupubs.onlinelibrary.wiley.com/doi/abs/10.1002/2014JA019961> doi: 10.1002/2014JA019961
- Le, G., Lühr, H., Anderson, B. J., Strangeway, R. J., Russell, C. T., Singer, H., ... Torbert, R. B. (2016). Magnetopause erosion during the 17 march 2015 magnetic storm: Combined field-aligned currents, auroral oval, and magnetopause observations. *Geophysical Research Letters*, *43*(6), 2396–2404. Retrieved from <https://agupubs.onlinelibrary.wiley.com/doi/abs/10.1002/2016GL068257> doi: 10.1002/2016GL068257
- Liemohn, M. W., Ganushkina, N. Y., De Zeeuw, D. L., Rastaetter, L., Kuznetsova, M., Welling, D. T., ... van der Holst, B. (2018). Real-time swmf at ccmc: Assessing the dst output from continuous operational simulations. *Space Weather*, *16*(10), 1583–1603. Retrieved from <https://agupubs.onlinelibrary.wiley.com/doi/abs/10.1029/2018SW001953> doi: 10.1029/2018SW001953
- Liemohn, M. W., McCollough, J. P., Jordanova, V. K., Ngwira, C. M., Morley, S. K., Cid, C., ... Vasile, R. (2018). Model evaluation guidelines for geomagnetic index predictions. *Space Weather*, *16*(12), 2079–2102. Retrieved from <https://agupubs.onlinelibrary.wiley.com/doi/abs/10.1029/2018SW002067> doi: 10.1029/2018SW002067
- Liemohn, M. W., Ridley, A. J., Brandt, P. C., Gallagher, D. L., Kozyra, J. U., Ober, D. M., ... DeMajistre, R. (2005, dec). Parametric analysis of nightside conductance effects on inner magnetospheric dynamics for the 17 April 2002 storm. *Journal of Geophysical Research*, *110*(A12), A12S22. Retrieved from

- 1017 <http://doi.wiley.com/10.1029/2005JA011109> doi: 10.1029/2005JA011109
 1018 Lu, G., Siscoe, G. L., Richmond, A. D., Pulkkinen, T. I., Tsyganenko, N. A.,
 1019 Singer, H. J., & Emery, B. A. (1997). Mapping of the ionospheric field-
 1020 aligned currents to the equatorial magnetosphere. *Journal of Geophysical*
 1021 *Research: Space Physics*, 102(A7), 14467–14476. Retrieved from [https://](https://agupubs.onlinelibrary.wiley.com/doi/abs/10.1029/97JA00744)
 1022 agupubs.onlinelibrary.wiley.com/doi/abs/10.1029/97JA00744 doi:
 1023 10.1029/97JA00744
- 1024 Merkin, V. G., Milikh, G., Papadopoulos, K., Lyon, J., Dimant, Y. S., Sharma,
 1025 A. S., ... Wiltberger, M. (2005, nov). Effect of anomalous electron heating on
 1026 the transpolar potential in the LFM global MHD model. *Geophysical Research*
 1027 *Letters*, 32(22), n/a–n/a. Retrieved from [http://doi.wiley.com/10.1029/](http://doi.wiley.com/10.1029/2005GL023315)
 1028 [2005GL023315](http://doi.wiley.com/10.1029/2005GL023315) doi: 10.1029/2005GL023315
- 1029 Merkin, V. G., Sharma, A. S., Papadopoulos, K., Milikh, G., Lyon, J., & Goodrich,
 1030 C. (2005, sep). Global MHD simulations of the strongly driven magnetosphere:
 1031 Modeling of the transpolar potential saturation. *Journal of Geophysical Research:*
 1032 *Space Physics*, 110(A9). Retrieved from [http://doi.wiley.com/10.1029/](http://doi.wiley.com/10.1029/2004JA010993)
 1033 [2004JA010993](http://doi.wiley.com/10.1029/2004JA010993) doi: 10.1029/2004JA010993
- 1034 Merkine, V. G., Papadopoulos, K., Milikh, G., Sharma, A. S., Shao, X., Lyon, J.,
 1035 & Goodrich, C. (2003, dec). Effects of the solar wind electric field and iono-
 1036 spheric conductance on the cross polar cap potential: Results of global MHD
 1037 modeling. *Geophysical Research Letters*, 30(23), n/a–n/a. Retrieved from
 1038 <http://doi.wiley.com/10.1029/2003GL017903> doi: 10.1029/2003GL017903
- 1039 Moen, J., & Brekke, A. (1993, may). The solar flux influence on quiet time con-
 1040 ductances in the auroral ionosphere. *Geophysical Research Letters*, 20(10), 971–
 1041 974. Retrieved from <http://doi.wiley.com/10.1029/92GL02109> doi: 10.1029/
 1042 [92GL02109](http://doi.wiley.com/10.1029/92GL02109)
- 1043 Morley, S. K., Brito, T. V., & Welling, D. T. (2018). Measures of Model Perfor-
 1044 mance Based On the Log Accuracy Ratio. *Space Weather*, 16(1), 69–88. Re-
 1045 trieved from [https://agupubs.onlinelibrary.wiley.com/doi/abs/10.1002/](https://agupubs.onlinelibrary.wiley.com/doi/abs/10.1002/2017SW001669)
 1046 [2017SW001669](https://agupubs.onlinelibrary.wiley.com/doi/abs/10.1002/2017SW001669) doi: 10.1002/2017SW001669
- 1047 Mukhopadhyay, A. (2017). *Statistical Comparison of Magnetopause Distances and*
 1048 *CPCP Estimation by Global MHD Models* (Tech. Rep.). Retrieved from [https://](https://ccmc.gsfc.nasa.gov/RoR/_WWW/SWREDI/contest-presentations/2017/Statistical_{_}Comparison_{_}of_{_}MP_{_}Distances_{_}and_{_}CPCP_{_}CCMC_{_}Contest_{_}2_{_}AgnitM.pdf)
 1049 [ccmc.gsfc.nasa.gov/RoR/_WWW/SWREDI/contest-presentations/2017/](https://ccmc.gsfc.nasa.gov/RoR/_WWW/SWREDI/contest-presentations/2017/Statistical_{_}Comparison_{_}of_{_}MP_{_}Distances_{_}and_{_}CPCP_{_}CCMC_{_}Contest_{_}2_{_}AgnitM.pdf)
 1050 [Statistical_{_}Comparison_{_}of_{_}MP_{_}Distances_{_}and_{_}CPCP_{_}CCMC_{_}Contest_{_}2_{_}AgnitM](https://ccmc.gsfc.nasa.gov/RoR/_WWW/SWREDI/contest-presentations/2017/Statistical_{_}Comparison_{_}of_{_}MP_{_}Distances_{_}and_{_}CPCP_{_}CCMC_{_}Contest_{_}2_{_}AgnitM.pdf)
 1051 [.pdf](https://ccmc.gsfc.nasa.gov/RoR/_WWW/SWREDI/contest-presentations/2017/Statistical_{_}Comparison_{_}of_{_}MP_{_}Distances_{_}and_{_}CPCP_{_}CCMC_{_}Contest_{_}2_{_}AgnitM.pdf) doi: <https://doi.org/10.1002/essoar.10502157.1>
- 1052 Mukhopadhyay, A., Welling, D., Burleigh, M., Ridley, A., Liemohn, M., Anderson,
 1053 B., & Gjerloev, J. (2019, dec). Conductance in the Aurora: Influence of Magneto-
 1054 spheric Contributors. In *Agu fall meeting abstracts* (Vol. 2019, pp. SA41B–3169).
 1055 Retrieved from [https://ui.adsabs.harvard.edu/abs/2019AGUFMSA41B3169M/](https://ui.adsabs.harvard.edu/abs/2019AGUFMSA41B3169M/abstract)
 1056 [abstract](https://ui.adsabs.harvard.edu/abs/2019AGUFMSA41B3169M/abstract) doi: doi.org/10.1002/essoar.10502150.1
- 1057 Mukhopadhyay, A., Welling, D., Liemohn, M., Zou, S., & Ridley, A. (2018, dec).
 1058 Challenges in Space Weather Prediction: Estimation of Auroral Conductance.
 1059 In *Agu fall meeting abstracts* (Vol. 2018, pp. SA33B–3462). Retrieved from
 1060 <https://ui.adsabs.harvard.edu/abs/2018AGUFMSA33B3462M/abstract>
- 1061 Newell, P. T., Sotirelis, T., & Wing, S. (2009, sep). Diffuse, monoenergetic, and
 1062 broadband aurora: The global precipitation budget. *Journal of Geophysical*
 1063 *Research: Space Physics*, 114(A9). Retrieved from [http://doi.wiley.com/](http://doi.wiley.com/10.1029/2009JA014326)
 1064 [10.1029/2009JA014326](http://doi.wiley.com/10.1029/2009JA014326) doi: 10.1029/2009JA014326
- 1065 Ohtani, S., Wing, S., Merkin, V. G., & Higuchi, T. (2014, jan). Solar cycle
 1066 dependence of nightside field-aligned currents: Effects of dayside ionospheric
 1067 conductivity on the solar wind-magnetosphere-ionosphere coupling. *Jour-*
 1068 *nal of Geophysical Research: Space Physics*, 119(1), 322–334. Retrieved from
 1069 <http://doi.wiley.com/10.1002/2013JA019410> doi: 10.1002/2013JA019410
- 1070 Ozturk, D. S., Zou, S., & Slavin, J. A. (2017). IMF By effects on ground mag-

- 1071 netometer response to increased solar wind dynamic pressure derived from
 1072 global MHD simulations. *Journal of Geophysical Research: Space Physics*. doi:
 1073 10.1002/2017JA023903
- 1074 Perlongo, N. J., Ridley, A. J., Liemohn, M. W., & Katus, R. M. (2017, apr). The
 1075 effect of ring current electron scattering rates on magnetosphere-ionosphere
 1076 coupling. *Journal of Geophysical Research: Space Physics*, *122*(4), 4168–
 1077 4189. Retrieved from <http://doi.wiley.com/10.1002/2016JA023679> doi:
 1078 10.1002/2016JA023679
- 1079 Powell, K. G., Roe, P. L., Linde, T. J., Gombosi, T. I., & Zeeuw, D. L. D.
 1080 (1999). A Solution-Adaptive Upwind Scheme for Ideal Magnetohydrodynam-
 1081 ics. *Journal of Computational Physics*, *154*(2), 284–309. Retrieved from
 1082 <http://www.sciencedirect.com/science/article/pii/S002199919996299X>
 1083 doi: <https://doi.org/10.1006/jcph.1999.6299>
- 1084 Pujol, J. (2007). The solution of nonlinear inverse problems and the Levenberg-
 1085 Marquardt method. *Geophysics*, *72*(4), W1–W16. Retrieved from [https://doi](https://doi.org/10.1190/1.2732552)
 1086 [.org/10.1190/1.2732552](https://doi.org/10.1190/1.2732552) doi: 10.1190/1.2732552
- 1087 Pulkkinen, A., Kuznetsova, M., Ridley, A., Raeder, J., Vapirev, A., Weimer, D.,
 1088 ... Chulaki, A. (2011, feb). Geospace Environment Modeling 2008-2009
 1089 Challenge: Ground magnetic field perturbations. *Space Weather*, *9*(2), n/a–
 1090 n/a. Retrieved from <http://doi.wiley.com/10.1029/2010SW000600> doi:
 1091 10.1029/2010SW000600
- 1092 Pulkkinen, A., Rastätter, L., Kuznetsova, M., Singer, H., Balch, C., Weimer, D., ...
 1093 Weigel, R. (2013, jun). Community-wide validation of geospace model ground
 1094 magnetic field perturbation predictions to support model transition to opera-
 1095 tions. *Space Weather*, *11*(6), 369–385. Retrieved from [http://doi.wiley.com/](http://doi.wiley.com/10.1002/swe.20056)
 1096 [10.1002/swe.20056](http://doi.wiley.com/10.1002/swe.20056) doi: 10.1002/swe.20056
- 1097 Raeder, J., McPherron, R. L., Frank, L. A., Kokubun, S., Lu, G., Mukai, T., ...
 1098 Slavin, J. A. (2001). Global simulation of the Geospace Environment Model-
 1099 ing substorm challenge event. *Journal of Geophysical Research-Space Physics*,
 1100 *106*(A1), 381–395. doi: 10.1029/2000ja000605
- 1101 Richmond, A. D., & Kamide, Y. (1988). Mapping electrodynamic features of the
 1102 high-latitude ionosphere from localized observations - Technique. *Journal of Geo-*
 1103 *physical Research*, *93*(A6), 5741–5759. doi: 10.1029/JA093iA06p05741
- 1104 Ridley, A. J., De Zeeuw, D. L., Gombosi, T. I., & Powell, K. G. (2001). Using
 1105 steady state MHD results to predict the global state of the magnetosphere-
 1106 ionosphere system. *Journal of Geophysical Research*, *106*(A12), 30067. Re-
 1107 trieved from <http://adsabs.harvard.edu/abs/2001JGR...10630067R> doi:
 1108 10.1029/2000JA002233
- 1109 Ridley, A. J., Gombosi, T. I., & De Zeeuw, D. L. (2004). Ionospheric control of the
 1110 magnetosphere: conductance. *Annales Geophysicae*, *22*(2), 567–584. Retrieved
 1111 from <https://hal.archives-ouvertes.fr/hal-00317238/> doi: 10.5194/angeo
 1112 -22-567-2004
- 1113 Ridley, A. J., Gombosi, T. I., Sokolov, I. V., Tóth, G., & Welling, D. T. (2010, aug).
 1114 Numerical considerations in simulating the global magnetosphere. *Annales Geo-*
 1115 *physicae*, *28*(8), 1589–1614. Retrieved from [http://www.ann-geophys.net/28/](http://www.ann-geophys.net/28/1589/2010/)
 1116 [1589/2010/](http://www.ann-geophys.net/28/1589/2010/) doi: 10.5194/angeo-28-1589-2010
- 1117 Ridley, A. J., & Liemohn, M. W. (2002, aug). A model-derived storm time
 1118 asymmetric ring current driven electric field description. *Journal of Geophys-*
 1119 *ical Research: Space Physics*, *107*(A8), SMP 2–1–SMP 2–12. Retrieved from
 1120 <http://doi.wiley.com/10.1029/2001JA000051> doi: 10.1029/2001JA000051
- 1121 Robinson, R. M., Vondrak, R. R., Miller, K., Dabbs, T., & Hardy, D. (1987,
 1122 mar). On calculating ionospheric conductances from the flux and energy
 1123 of precipitating electrons. *Journal of Geophysical Research*, *92*(A3), 2565.
 1124 Retrieved from <http://doi.wiley.com/10.1029/JA092iA03p02565> doi:

- 1125 10.1029/JA092iA03p02565
- 1126 Robinson, R. M., Zhang, Y., Anderson, B. J., Zanetti, L. J., Korth, H., & Fitzmaurice, A. (2018). Statistical relations between field-aligned currents and precipitating electron energy flux. *Geophysical Research Letters*, *45*(17), 8738–8745. Retrieved from <https://agupubs.onlinelibrary.wiley.com/doi/abs/10.1029/2018GL078718> doi: 10.1029/2018GL078718
- 1130
- 1131 Roederer, J. G. (1970). *Dynamics of Geomagnetically Trapped Radiation (Vol. 2)*. Berlin, Heidelberg: Springer Berlin Heidelberg. doi: <https://doi.org/10.1007/978-3-642-49300-3>
- 1132
- 1133
- 1134 Schunk, R., & Nagy, A. (2009). *Ionospheres: Physics, Plasma Physics, and Chemistry* (2nd ed.). Cambridge University Press. doi: 10.1017/CBO9780511635342
- 1135
- 1136 Sorkine, O., Cohen-Or, D., Lipman, Y., Alexa, M., Rössl, C., & Seidel, H.-P. (2004). Laplacian surface editing. In *Proceedings of the 2004 eurographics/acm siggraph symposium on geometry processing* (p. 175–184). New York, NY, USA: Association for Computing Machinery. Retrieved from <https://doi.org/10.1145/1057432.1057456> doi: 10.1145/1057432.1057456
- 1137
- 1138
- 1139
- 1140
- 1141 Tóth, G., Meng, X., Gombosi, T. I., & Rastätter, L. (2014). Predicting the time derivative of local magnetic perturbations. *Journal of Geophysical Research: Space Physics*, *119*(1), 310–321. Retrieved from <https://agupubs.onlinelibrary.wiley.com/doi/abs/10.1002/2013JA019456> doi: 10.1002/2013JA019456
- 1142
- 1143
- 1144
- 1145 Tóth, G., Sokolov, I. V., Gombosi, T. I., Chesney, D. R., Clauer, C. R., De Zeeuw, D. L., ... Kóta, J. (2005, dec). Space Weather Modeling Framework: A new tool for the space science community. *Journal of Geophysical Research*, *110*(A12), A12226. Retrieved from <http://doi.wiley.com/10.1029/2005JA011126> doi: 10.1029/2005JA011126
- 1146
- 1147
- 1148
- 1149
- 1150 Tóth, G., van der Holst, B., Sokolov, I. V., De Zeeuw, D. L., Gombosi, T. I., Fang, F., ... Opher, M. (2012). Adaptive numerical algorithms in space weather modeling. *Journal of Computational Physics*, *231*(3), 870–903. doi: 10.1016/j.jcp.2011.02.006
- 1151
- 1152
- 1153
- 1154 Waters, C. L., Anderson, B. J., Green, D. L., Korth, H., Barnes, R. J., & Vanhamäki, H. (2020). Science data products for ampere. In M. W. Dunlop & H. Lühr (Eds.), *Ionospheric multi-spacecraft analysis tools: Approaches for deriving ionospheric parameters* (pp. 141–165). Cham: Springer International Publishing. Retrieved from https://doi.org/10.1007/978-3-030-26732-2_7 doi: 10.1007/978-3-030-26732-2_7
- 1155
- 1156
- 1157
- 1158
- 1159
- 1160 Welling, D. T. (2019). Magnetohydrodynamic models of b and their use in gic estimates. In *Geomagnetically induced currents from the sun to the power grid* (p. 43–65). American Geophysical Union (AGU). Retrieved from <https://agupubs.onlinelibrary.wiley.com/doi/abs/10.1002/9781119434412.ch3> doi: 10.1002/9781119434412.ch3
- 1161
- 1162
- 1163
- 1164
- 1165 Welling, D. T., Anderson, B. J., Crowley, G., Pulkkinen, A. A., & Rastätter, L. (2017, jan). Exploring predictive performance: A reanalysis of the geospace model transition challenge. *Space Weather*, *15*(1), 192–203. Retrieved from <http://doi.wiley.com/10.1002/2016SW001505> doi: 10.1002/2016SW001505
- 1166
- 1167
- 1168
- 1169 Welling, D. T., Ngwira, C. M., Opgenoorth, H., Haiducek, J. D., Savani, N. P., Morley, S. K., ... Liemohn, M. (2018). Recommendations for next-generation ground magnetic perturbation validation. *Space Weather*, *16*(12), 1912–1920. Retrieved from <https://agupubs.onlinelibrary.wiley.com/doi/abs/10.1029/2018SW002064> doi: 10.1029/2018SW002064
- 1170
- 1171
- 1172
- 1173
- 1174 Welling, D. T., & Ridley, A. J. (2010). Exploring sources of magnetospheric plasma using multispecies MHD. *Journal of Geophysical Research: Space Physics*, *115*(A4). Retrieved from <https://agupubs.onlinelibrary.wiley.com/doi/abs/10.1029/2009JA014596> doi: 10.1029/2009JA014596
- 1175
- 1176
- 1177
- 1178 Wilks, D. S. (2011). *Statistical methods in the atmospheric sciences* (3rd ed.). Aca-

- 1179 demic Press.
- 1180 Wiltberger, M., Merkin, V., Zhang, B., Toffoletto, F., Oppenheim, M., Wang,
1181 W., ... Stephens, G. K. (2017, may). Effects of electrojet turbulence on
1182 a magnetosphere-ionosphere simulation of a geomagnetic storm. *Journal of*
1183 *Geophysical Research: Space Physics*, 122(5), 5008–5027. Retrieved from
1184 <http://doi.wiley.com/10.1002/2016JA023700> doi: 10.1002/2016JA023700
- 1185 Wiltberger, M., Wang, W., Burns, A. G., Solomon, S. C., Lyon, J. G., & Goodrich,
1186 C. C. (2004). Initial results from the coupled magnetosphere ionosphere ther-
1187 mosphere model: magnetospheric and ionospheric responses. *Journal of At-*
1188 *mospheric and Solar-Terrestrial Physics*, 66(15), 1411–1423. Retrieved from
1189 <http://www.sciencedirect.com/science/article/pii/S136468260400149X>
1190 doi: <https://doi.org/10.1016/j.jastp.2004.03.026>
- 1191 Wiltberger, M., Weigel, R. S., Lotko, W., & Fedder, J. A. (2001). Modeling sea-
1192 sonal variations of auroral particle precipitation in a global-scale magnetosphere-
1193 ionosphere simulation. *Journal of Geophysical Research-Space Physics*, 114(A1),
1194 381–395. doi: 10.1029/2008JA013108
- 1195 Wolf, R. A., Harel, M., Spiro, R. W., Voigt, G.-H., Reiff, P. H., & Chen, C.-K.
1196 (1982, aug). Computer simulation of inner magnetospheric dynamics for the
1197 magnetic storm of July 29, 1977. *Journal of Geophysical Research*, 87(A8),
1198 5949. Retrieved from <http://doi.wiley.com/10.1029/JA087iA08p05949> doi:
1199 10.1029/JA087iA08p05949
- 1200 Yagou, H., Ohtake, Y., & Belyaev, A. (2002, July). Mesh smoothing via mean and
1201 median filtering applied to face normals. In *Geometric modeling and processing.*
1202 *theory and applications. gmp 2002. proceedings* (p. 124–131). doi: 10.1109/GMAP
1203 .2002.1027503
- 1204 Yu, Y., Jordanova, V. K., Ridley, A. J., Albert, J. M., Horne, R. B., & Jef-
1205 fery, C. A. (2016). A new ionospheric electron precipitation module cou-
1206 pled with ram-scb within the geospace general circulation model. *Journal*
1207 *of Geophysical Research: Space Physics*, 121(9), 8554–8575. Retrieved from
1208 <https://agupubs.onlinelibrary.wiley.com/doi/abs/10.1002/2016JA022585>
1209 doi: 10.1002/2016JA022585
- 1210 Yu, Y., Ridley, A. J., Welling, D. T., & Tóth, G. (2010, aug). Including gap re-
1211 gion field-aligned currents and magnetospheric currents in the MHD calculation
1212 of ground-based magnetic field perturbations. *Journal of Geophysical Research:*
1213 *Space Physics*, 115(A8). Retrieved from [http://doi.wiley.com/10.1029/](http://doi.wiley.com/10.1029/2009JA014869)
1214 [2009JA014869](http://doi.wiley.com/10.1029/2009JA014869) doi: 10.1029/2009JA014869
- 1215 Zhang, B., Lotko, W., Brambles, O., Wiltberger, M., & Lyon, J. (2015). Elec-
1216 tron precipitation models in global magnetosphere simulations. *Journal of*
1217 *Geophysical Research: Space Physics*, 120(2), 1035–1056. Retrieved from
1218 <https://agupubs.onlinelibrary.wiley.com/doi/abs/10.1002/2014JA020615>
1219 doi: 10.1002/2014JA020615

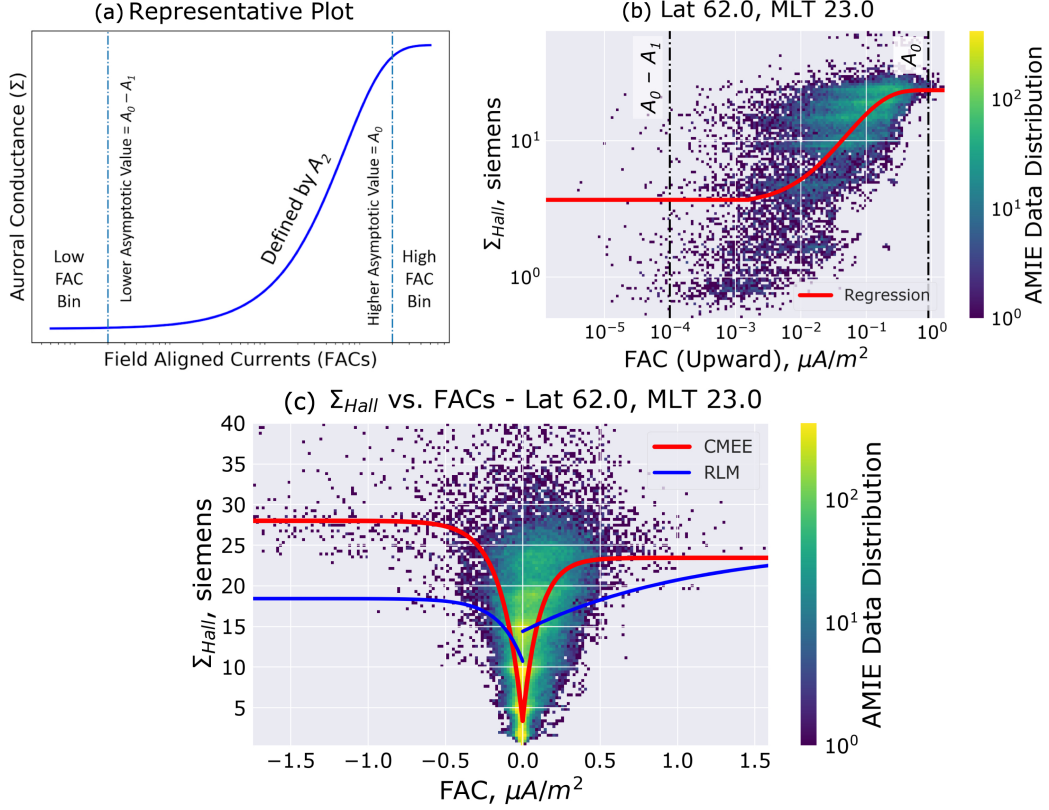


Figure 3. Example Fitting of the Conductance Model for Extreme Events (CMEE) - (a) Representative Line Plot of Auroral Conductance (Hall or Pedersen, in siemens) vs. Field Aligned Currents (FACs, Upward or Downward, in $\mu A/m^2$) through Equation 1 denoting the three regions of interest - low and high FAC bins used to estimate the values of A_0 and A_1 , while the region in between these bins defining the curve using regression of A_2 . (b) An example log-log plot of the AMIE data showing the scatter of Hall Conductance versus Upward Field Aligned Currents, at magnetic latitude of 68° and magnetic local time (MLT) 23 in the nightside auroral zone. Alongside the data spread, the regression line is plotted in red with the dot-dashed lines exhibiting the low and high FAC bins. (c) The distribution of AMIE data from 2003 showing the scatter of Hall Conductance versus all Field Aligned Currents plotted along the line plots of RLM and CMEE, denoted in blue and red respectively, at 68° magnetic latitude and 23 MLT. Note this distribution plot is in linear scale compared to the similar plot part (b), which is in logarithmic scale.

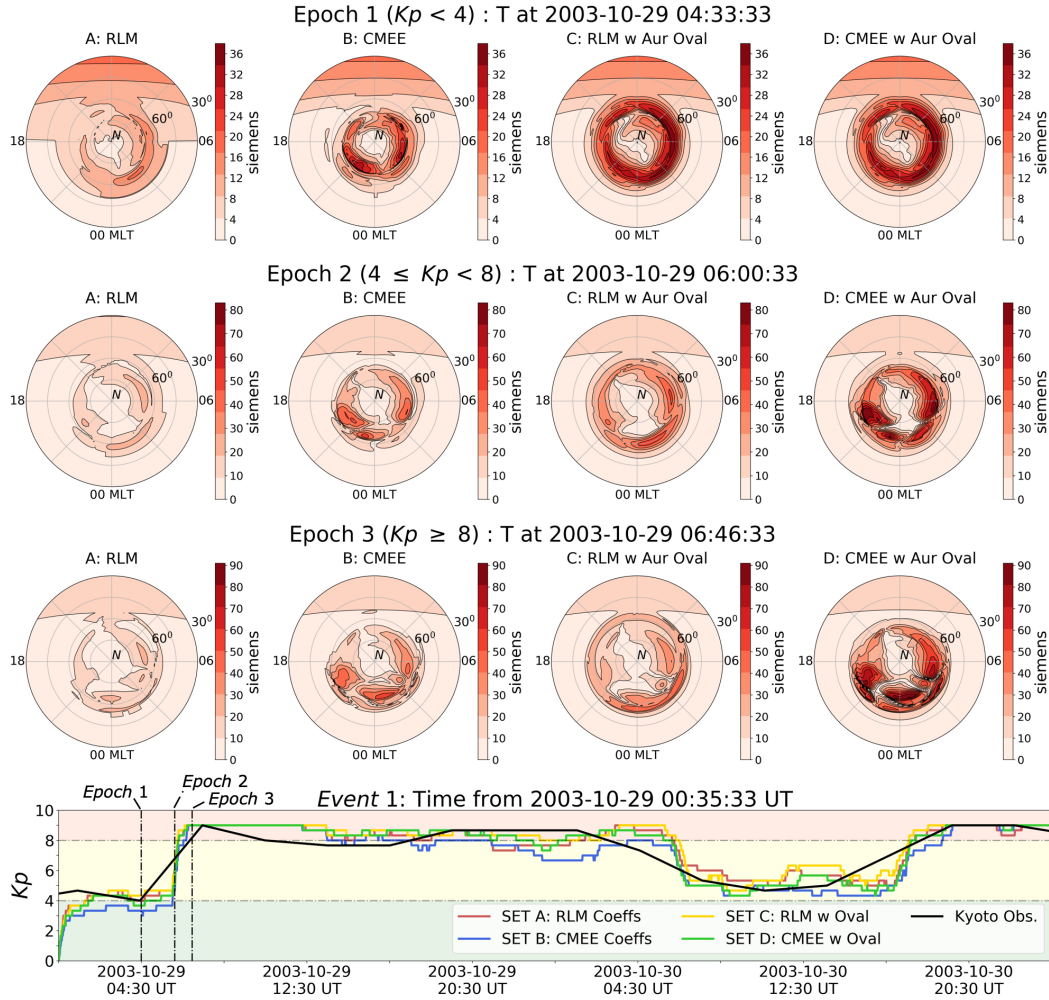


Figure 4. A comparison of Hall conductance values from different conductance model variants. Dial plots from (left to right) simulation sets A, B, C and D at time instances during Event 1 (Epoch 1, Top Row) when $Kp < 4$, (Epoch 2, Second Row) when $4 \leq Kp < 8$, and (Epoch 3, Third Row) when $Kp \geq 8$. (Bottom Subplot) Comparison of Kp from the Kyoto Observatory (in black) against simulated Kp from simulationsets A (in red), B (in blue), C (in gold) and D (in green). Additionally, the plot background is coloured by the Kp , green signifying $Kp < 4$, yellow signifying $4 \leq Kp < 8$, and red signifying $Kp \geq 8$.

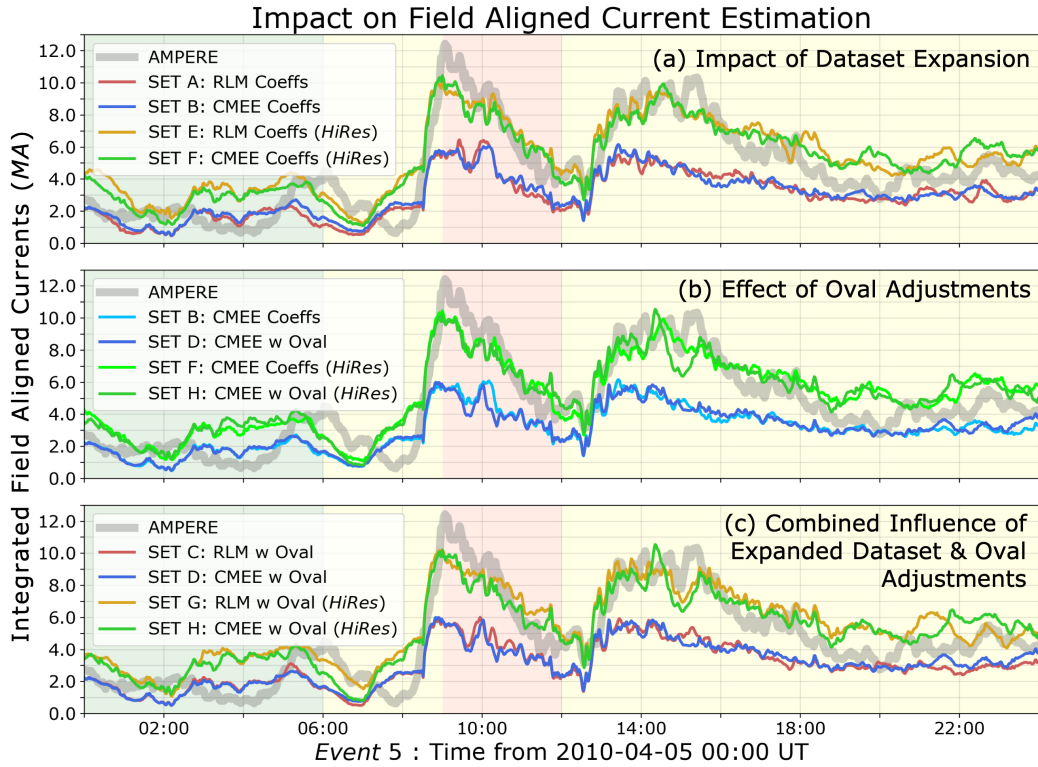


Figure 5. Time series comparison of integrated field aligned currents (iFACs) for Events 5 spanning the storm main phase from AMPERE (gray line) and the eight simulation sets of the SWMF. Goal of each frame: Top Frame (a) illustrates the impact of dataset expansion on iFACs by comparing Sets A (in red), B (in blue), E (in gold) and D (in green). Middle Frame (b) displays the effect of oval adjustments by comparing Sets B (in light blue), D (in blue), F (in light green) and H (in green). Bottom Frame (c) presents the combined influence of dataset expansion and oval adjustments by comparing Sets C (in red), D (in blue), G (in gold) and H (in green). The plot background is coloured by the Kp , green signifying $Kp < 4$, yellow signifying $4 \leq Kp < 8$, and red signifying $Kp \geq 8$.

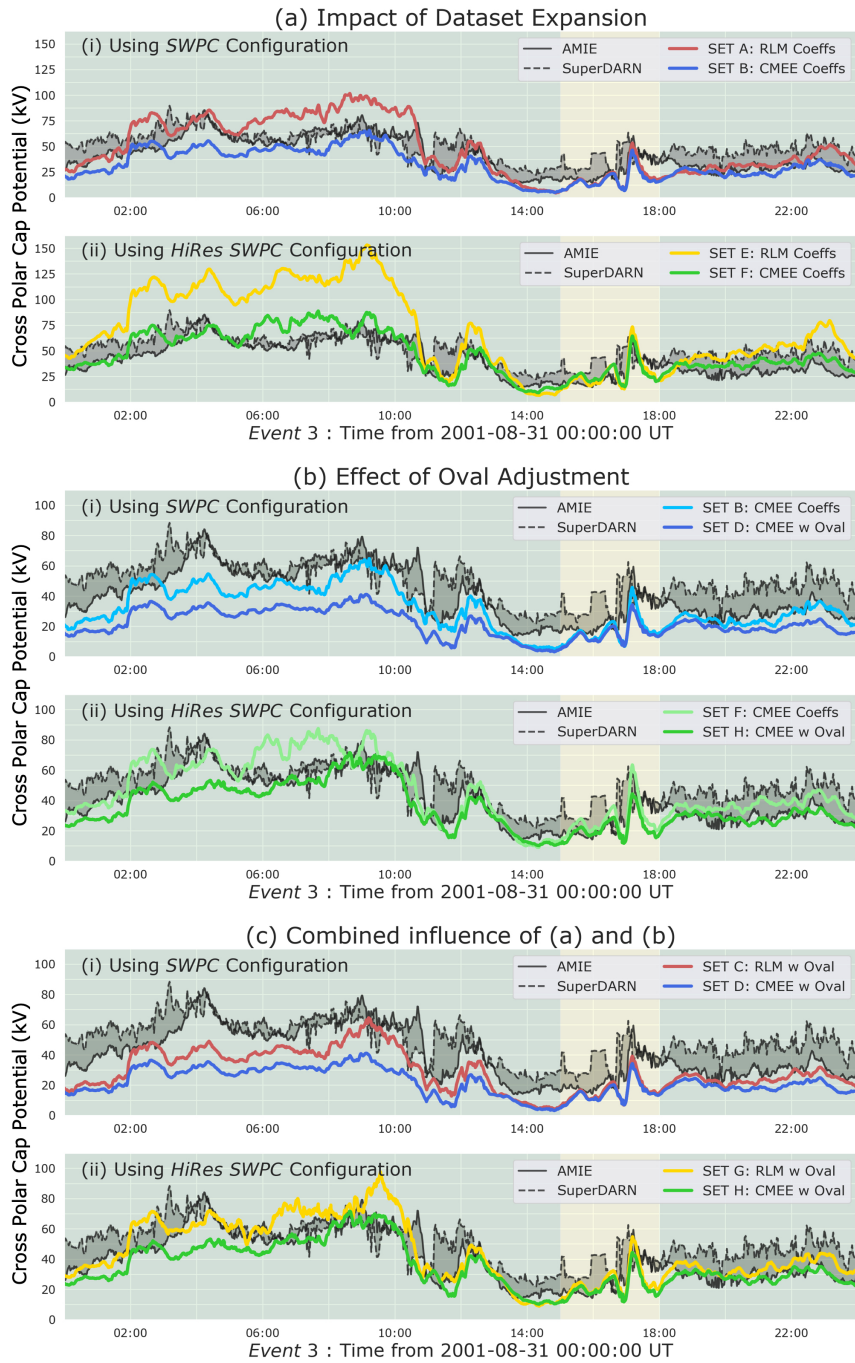


Figure 6. Time series comparison of cross polar cap potential (CPCP) for Event 3 comparing observations from AMIE, SuperDARN, and the eight configurations of the SWMF. Traces show AMIE in solid black, SuperDARN in dashed black, with the difference region between the datasets coloured gray. The SWMF simulations are coloured similarly to Figure 5. Goal of each frame: Top Frame (a) illustrates the impact of dataset expansion on iFACs by comparing (i) Sets A & B in upper panel, and (ii) Sets E & D in bottom panel. Middle Frame (b) displays the effect of oval adjustments by comparing (i) Sets B & D in upper panel, and (ii) F & H (in green) in bottom panel. Bottom Frame (c) presents the combined influence of dataset expansion and oval adjustments by comparing (i) Sets C & D in top panel, and (ii) G & H in bottom panel. The plot background is coloured by the Kp , green signifying $Kp < 4$, and yellow signifying $4 \leq Kp < 8$.

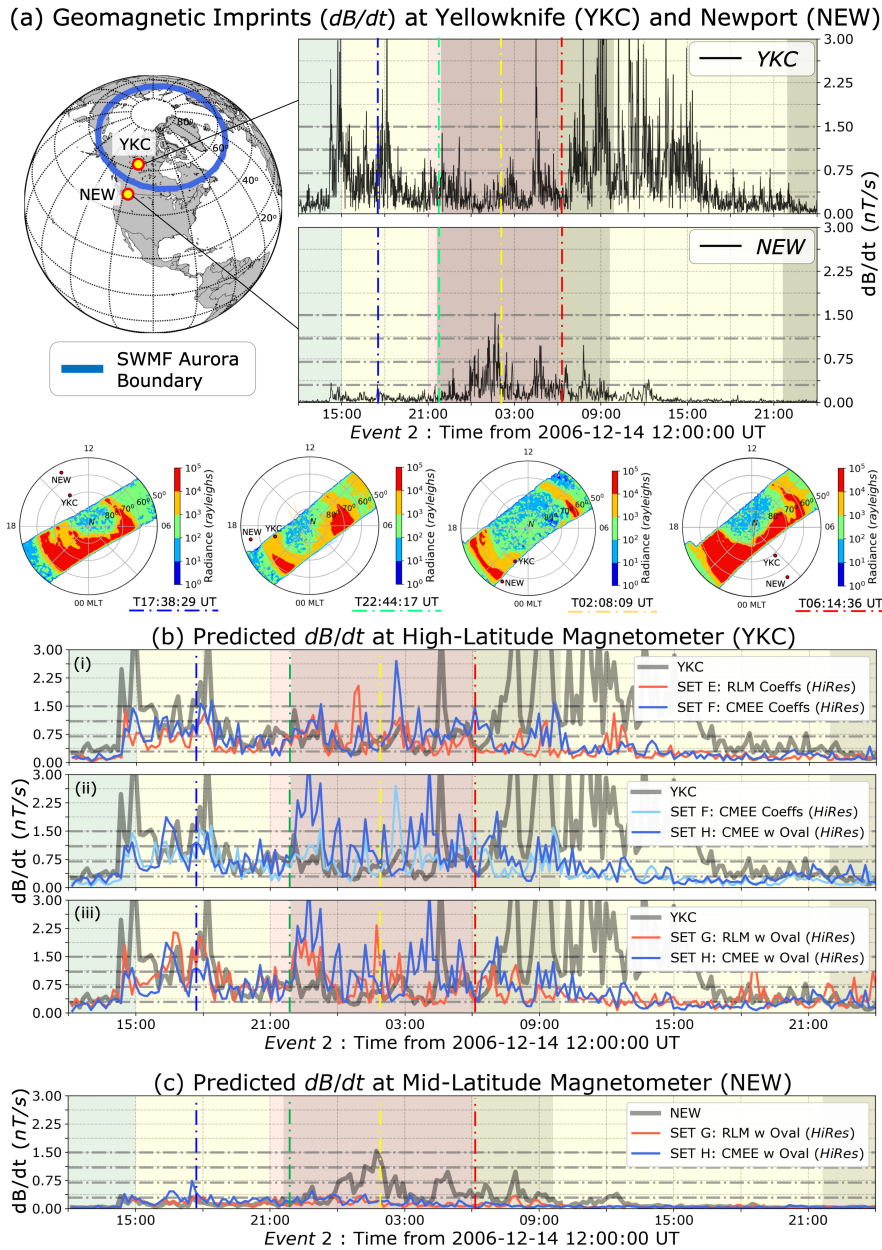
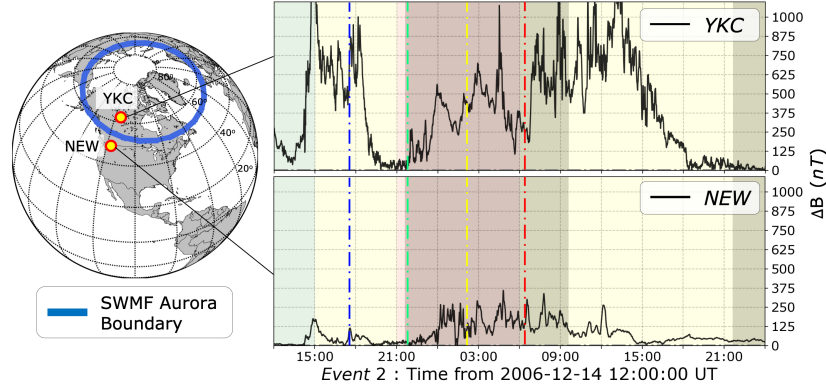
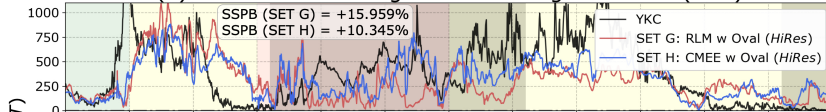


Figure 7. Impact of changes to the auroral conductance on dB/dt predictions - (a) (Left) Location of Yellowknife (YKC) and Newport (NEW) magnetometer stations mapped in geographic coordinates with the SWMF auroral boundary demarcated using the thick blue line. (Right) Raw dB/dt observations at a 1-minute cadence at YKC and NEW. (Bottom) Expansion of the auroral oval as seen through DMSF F16 auroral radiance maps and the magnetometer stations at Yellowknife (YKC) and Newport (NEW). The dialplots on top are demarcated by blue, green, yellow and red dot-dashed lines in the line plots, in increasing order of their timestamps. (b) Comparison of max-filtered predicted dB/dt from *Hi-Res* SWMF simulations against similarly filtered dB/dt observations at Yellowknife (YKC). Goal of each panel: Top panel (i) shows impact of coefficients by comparing simulation sets E (in red) and F (in blue). Middle panel (ii) illustrates the impact of oval adjustments by comparing sets F (in light blue) and H (in blue). Bottom panel (iii) compares sets G (in red) and H (in blue). Observations are shown as a thick, grey curve. (c) Comparison of max-filtered predicted dB/dt from sets G (in red) and H (in blue) against observations (thick, grey curve). The dot-dashed lines in the line plots are markers of the thresholds used in the *Pulkkinen2013* study for their event-based analysis. The background of the line plots are coloured by Kp , similarly to Figure 5. The dark shaded background regions are times when the respective magnetometer was in the nightside.

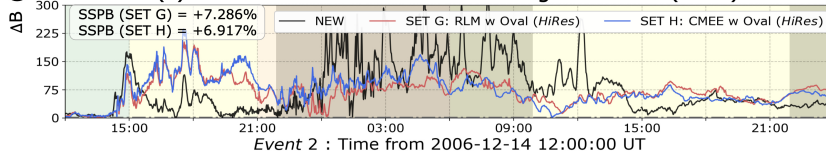
(a) Geomagnetic Imprints (ΔB) at Yellowknife (YKC) and Newport (NEW)



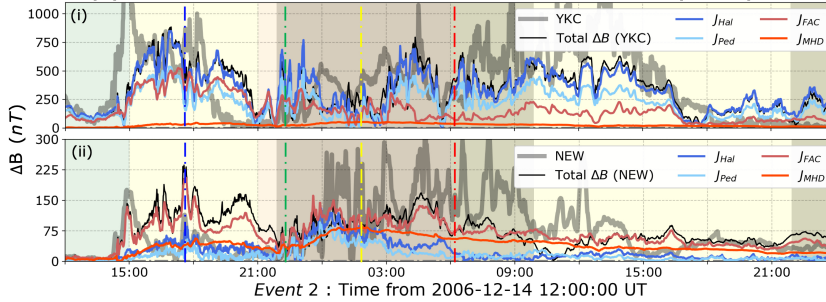
(b) Predicted ΔB at High-Latitude Magnetometer (YKC)



(c) Predicted ΔB at Mid-Latitude Magnetometer (NEW)



(d) Individual Current Contributions to simulated ΔB (CMEE)



(e) Modelled FACs and Hall Conductance (CMEE)

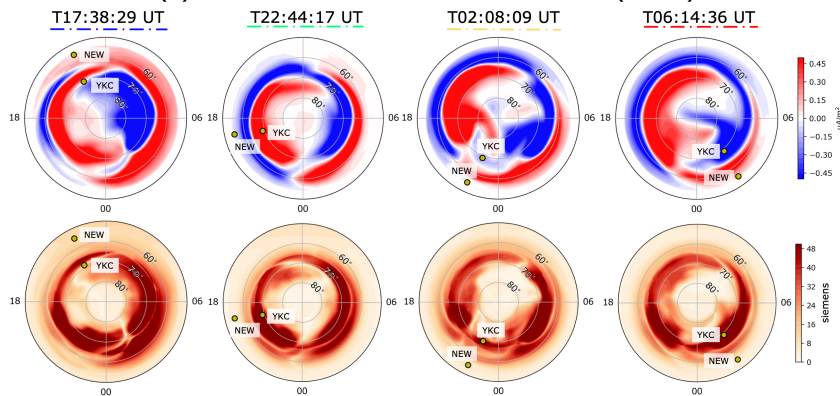


Figure 8. Impact of changes to the auroral conductance on ΔB predictions - (a) (Left) Location of Yellowknife (YKC) and Newport (NEW) magnetometer stations mapped in geographic coordinates with the SWMF auroral boundary demarcated using the thick blue line. (Right) Raw ΔB observations at a 1-minute cadence at YKC and NEW. (b) Comparison of predicted ΔB from *Hi-Res* SWMF simulations against observations at YKC, and (c) at NEW. Both subplots compare results from simulation sets G (in red) and H (in blue) against observations (in black). (d) Comparing contribution of individual current sources in the simulated ΔB at (i) YKC and (ii) NEW. The contributions from Hall currents are in blue, Pedersen currents in light blue, FACs in red, and MHD in orange. The background of the line plots are coloured by Kp , similarly to Figure 5. The dark shaded background regions are times when the respective magnetometer was in the nightside. (e) Dial plots of modelled FACs (top row) and Hall Conductance (bottom row) in the Northern hemisphere from simulation set H at the same time instances as the DMSF passes in Figure 7.

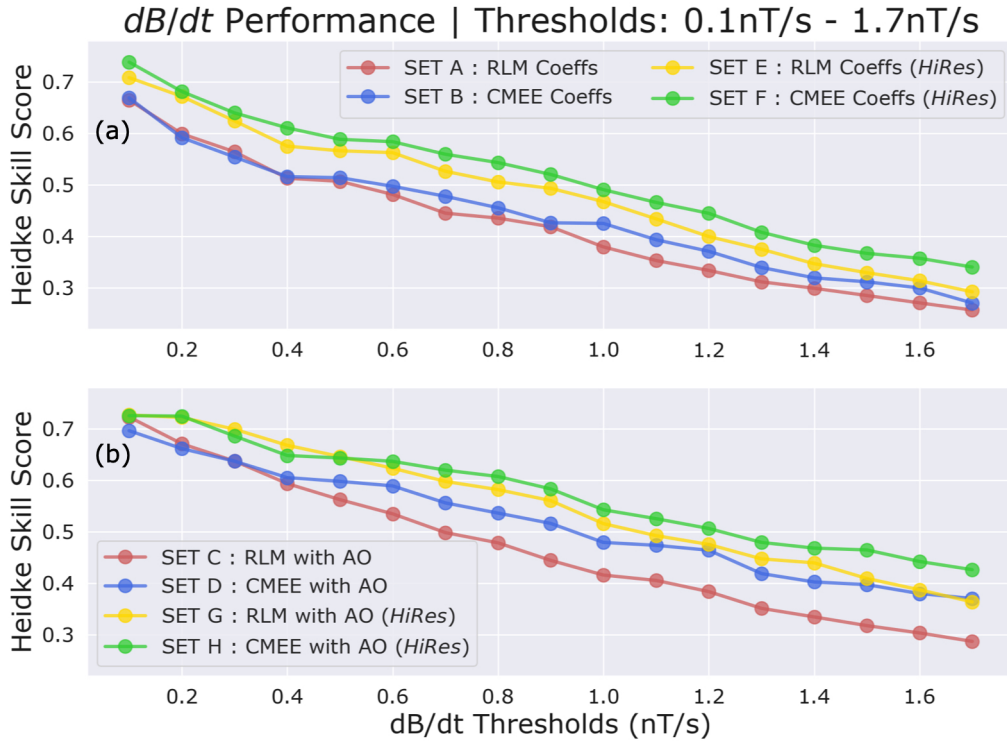


Figure 9. Heidke Skill Score (HSS) Performance of all SWMF simulation variants at ascending dB/dt predictions for all events from Table 1(a). (a) Comparison of simulation sets A (in red), B (in blue), E (in yellow) and F (in green) illustrating the impact of dataset expansion. (b) Comparison of simulation sets C (in red), D (in blue), G (in yellow) and H (in green) displaying the overall impact of dataset expansion with oval adjustments. Note the y-axis in (a) and (c) does not start at zero.

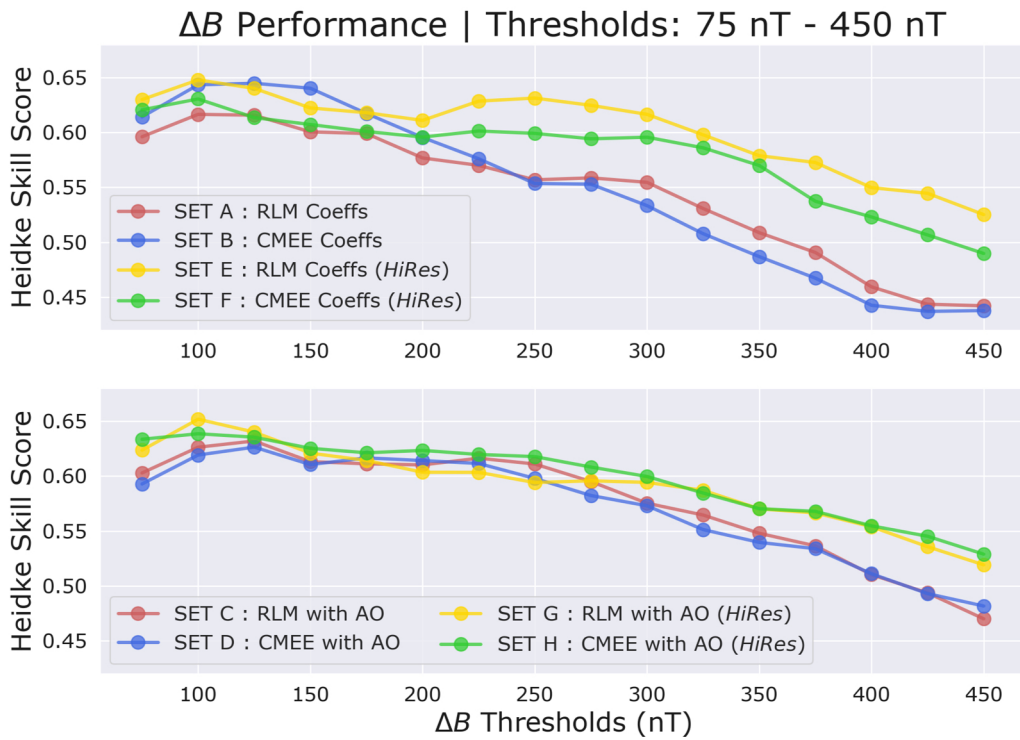


Figure 10. HSS Performance metrics of all SWMF simulation variants at ascending ΔB predictions for all events from Table 1(a). The format is similar to Figure 9. Note the y-axis in (a) and (c) does not start at zero, and spans a smaller range than Figures 9(a) and (c).